

Sterile Neutrino Fits to Short Baseline Neutrino Oscillation Measurements

*J.M. Conrad*¹, *C.M. Ignarra*¹, *G. Karagiorgi*², *M.H. Shaevitz*², *J. Spitz*¹

Abstract:

This paper reviews short baseline oscillation experiments as interpreted within the context of one, two, and three sterile neutrino models associated with additional neutrino mass states in the ~ 1 eV range. Appearance and disappearance signals and limits are considered. We show that fitting short baseline data sets to a (3+3) model, defined by three active and three sterile neutrinos, results in an overall goodness of fit of 67%, and a compatibility of 90% among all data sets – to be compared to the compatibility of 0.043% and 13% for a (3+1) and a (3+2) model, respectively. While the (3+3) fit yields the highest quality overall, it still finds inconsistencies with the MiniBooNE appearance data sets; in particular, the global fit fails to account for the observed MiniBooNE low-energy excess. Given the overall improvement, we recommend using the results of (3+2) and (3+3) fits, rather than (3+1) fits, for future neutrino oscillation phenomenology. These results motivate the pursuit of further short baseline experiments, such as those reviewed in this paper.

1 Introduction

Over the past 15 years, neutrino oscillations associated with small splittings between the neutrino mass states have become well established [1–16]. Based on this, a phenomenological extension of the Standard Model (SM) has been constructed involving three neutrino mass states, over which the three known flavors of neutrinos (ν_e , ν_μ and ν_τ) are distributed. This is a minimal extension of the SM, requiring a lepton mixing matrix that is analogous to the quark sector, and introducing neutrino mass.

Despite its success, the model does not address fundamental questions such as how neutrino masses should be incorporated into a SM Lagrangian, or why the neutrino sector has small masses and large mixing angles compared to the quark sector. As a result, while this structure makes successful predictions, one would like to gain a deeper understanding of neutrino phenomenology. This has led to searches for other unexpected properties of neutrinos that might lead to clues towards a more complete theory governing their behavior.

Recalling that the mass splitting is related to the frequency of oscillation, short baseline (SBL) experiments search for evidence of “rapid” oscillations above the established solar ($\sim 10^{-5}$ eV²) and atmospheric ($\sim 10^{-3}$ eV²) mass splittings that are incorporated into today’s framework. A key motivation is the search for light sterile neutrinos—fermions that do not participate in SM interactions but participate in mixing with the established SM neutrinos. Indications of oscillations between active and sterile neutrinos have been observed in the LSND [17], MiniBooNE [18] and reactor [19] experiments, though many others have contributed additional probes of the effect, which are of comparable sensitivity and/or complementary to those above.

This paper examines these results within the context of models describing oscillations with sterile neutrinos. An oscillation formalism that introduces multiple sterile neutrinos is described in the next section. Following this, we review the SBL data sets used in the fits presented in this paper, which

¹Massachusetts Institute of Technology, Cambridge, MA 02139, USA

²Columbia University, New York, NY 10027, USA

include both positive signals and stringent limits. We then detail the analysis approach, which we have developed in a series of past papers [20–22]. The global fits are presented with one, two, and three light sterile neutrinos. While groups [20, 23, 24] have explored fits with three sterile neutrinos in the past, the fits presented here represent an important step forward. Specifically, we show that, for the first time, the (3+3) model resolves some disagreements between the data sets and substantially improves the overall goodness of fit as compared to the (3+2) model. Lastly, the future of SBL searches for sterile neutrinos is reviewed.

2 Oscillations Involving Sterile Neutrinos

2.1 Light Sterile States

Sterile neutrinos are additional states beyond the standard electron, muon, and tau flavors, which do not interact via the exchange of W or Z bosons [25] and are thus “sterile” with respect to the weak interaction. These states are motivated by many Beyond Standard Model theories, where they are often introduced as gauge singlets. Traditionally, sterile neutrinos were introduced at very high mass scales within the context of grand unification and leptogenesis. For many years, sterile neutrinos with light masses were regarded as less natural. However, as recent data [17, 19, 26, 27] has indicated the potential existence of light sterile neutrinos, the theoretical view has evolved to accommodate these light mass gauge singlets. At this point, it is generally accepted that the mass scale for sterile neutrinos is not well predicted, and the existence of one or more sterile neutrinos accommodated by introducing extra neutrino mass states at the eV scale is possible. An excellent review of the phenomenology of sterile neutrinos, as well as the data motivating light sterile models, is provided in Ref. [23].

Within the expanded oscillation phenomenology, sterile neutrinos are handled as additional non-interacting flavors, which are connected to additional mass states via an extended mixing matrix with extra mixing angles and possible CP violation phases. These additional mass states must be mostly sterile, with only a small admixture of the active flavors, in order to accommodate the limits on oscillations to sterile neutrinos from the atmospheric and solar neutrino data. Experimental evidence for these additional mass states would come from the disappearance of an active flavor to a sterile neutrino state or additional transitions from one active flavor to another through the sterile neutrino state.

The number of light sterile neutrinos is not predicted by theory. However, a natural tendency is to introduce three sterile states. Depending on how the states are distributed in mass scale, one, two, or all three states may be involved in SBL oscillations. These are referred to as (3+N) models where the “3” refers to the three active flavors and the “N” refers to the number of sterile neutrinos.

Introducing sterile neutrinos can have implications in cosmological observations, especially measurements of the radiation density in the early universe. These are compounded if the extra neutrinos have significant mass (>1 eV) and do not decay. Currently, cosmological data allow additional states. For example, Ref. [28] estimates the effective number of neutrinos to be $N_{eff} = 5.3 \pm 1.3$. Similar cosmological-based analyses favoring light sterile neutrinos can be found in Refs. [29] and [30]. Upcoming Planck data [31] is expected to precisely measure N_{eff} . This parameter, however, can be considered a model dependent one. As an example, there are a variety of classes of theories where the neutrinos do not thermalize in the early universe [23]. In these cases, the cosmological neutrino abundance would substantially decrease, rendering cosmological measurements of N_{eff} invalid. Therefore, while the community certainly looks forward to cosmological measurements of N_{eff} , we think that

SBL experiments are a largely better approach for probing sterile neutrinos and constraining their mixing properties. We therefore proceed with a study of the SBL data, without further reference to the cosmological results.

2.2 The Basic Oscillation Formalism

Before considering the phenomenology of light sterile neutrinos, it is useful to introduce the idea of oscillations within a simpler model. In this section, we first consider the two-neutrino formalism. We then extend these ideas to form the well established three-active-flavor neutrino model. Based on these concepts, we expand the discussion to include more states in the following section.

Neutrino oscillations require that 1) neutrinos have mass; 2) the difference between the masses is small; and 3) the mass eigenstates are rotations of the weak interaction eigenstates. These rotations are given in a simple two-neutrino model as:

$$\begin{aligned}\nu_e &= \cos \theta \nu_1 + \sin \theta \nu_2 \\ \nu_\mu &= -\sin \theta \nu_1 + \cos \theta \nu_2 ,\end{aligned}$$

where ν_i ($i = 1, 2$) is the “mass eigenstate”, ν_α ($\alpha = e, \mu$) is the “flavor eigenstate”, and θ is the “mixing angle”. Under these conditions, a neutrino born in a pure flavor state through a weak decay can oscillate into another flavor as the state propagates in space, due to the fact that the different mass eigenstate components propagate with different frequencies. The mass splitting between the two states is $\Delta m^2 = |m_2^2 - m_1^2| > 0$. The oscillation probability for $\nu_\mu \rightarrow \nu_e$ oscillations is then given by:

$$P(\nu_\mu \rightarrow \nu_e) = \sin^2 2\theta \sin^2 \left(\frac{1.27 \Delta m^2 (\text{eV}^2) L (\text{km})}{E (\text{GeV})} \right) , \quad (1)$$

where L is the distance from the source, and E is the neutrino energy.

From Eq. 1, one can see that the probability for observing oscillations is large when $\Delta m^2 \sim E/L$. In the discussions below, we will focus on experiments with signals in the $\Delta m^2 \sim 1 \text{ eV}^2$ range. These experiments are therefore designed with $E/L \sim 1 \text{ GeV/km}$ (or, alternatively, 1 MeV/m). Typically, neutrino source energies range from a few MeV to a few GeV. Thus, most of the experiments considered are located between a few meters and a few kilometers from the source. This is not absolutely necessary—a very high energy experiment with a very long baseline is sensitive to oscillations in the $\Delta m^2 \sim 1 \text{ eV}^2$ range, as long as the ratio $E/L \sim 1 \text{ GeV/km}$ is maintained. In other words, “short baseline experiments” is something of a misnomer – what is meant is experiments with sensitivity to $\Delta m^2 \sim 1 \text{ eV}^2$ oscillations.

In the case where $E/L \ll 1 \text{ GeV/km}$, such as in accelerator based experiments with long baselines (hundreds of kilometers), one can see from Eq. 1 that the oscillations will be rapid. In the case of $\Delta m^2 \sim 1 \text{ eV}^2$, sensitivity to the mass splitting is lost because the $\sin^2(1.27\Delta m^2(L/E))$ term will average to $1/2$ due to the finite energy and position resolution of the experiment. The oscillation probability becomes $P = (\sin^2 2\theta)/2$ in this case. Thus, the information from “long baseline experiments” can be used to constrain the mixing angle, but not the Δm^2 .

The exercise of generalizing to a three-neutrino model is useful, since the inclusion of more states follows from this procedure. Within a three-neutrino model, the mixing matrix is written as:

$$\begin{pmatrix} \nu_e \\ \nu_\mu \\ \nu_\tau \end{pmatrix} = \begin{pmatrix} U_{e1} & U_{e2} & U_{e3} \\ U_{\mu1} & U_{\mu2} & U_{\mu3} \\ U_{\tau1} & U_{\tau2} & U_{\tau3} \end{pmatrix} \begin{pmatrix} \nu_1 \\ \nu_2 \\ \nu_3 \end{pmatrix} .$$

The matrix elements are parametrized by three mixing angles, analogous to the Euler angles. As in the quark sector, the three-neutrino model can be extended to include an imaginary term that introduces a CP-violating phase. This formalism is analogous to the quark sector, where strong and weak eigenstates are rotated and the resultant mixing is described conventionally by a unitary mixing matrix.

The oscillation probability for three-neutrino oscillations is typically written as:

$$P(\nu_\alpha \rightarrow \nu_\beta) = \delta_{\alpha\beta} - 4 \sum_{j>i} U_{\alpha i} U_{\beta i}^* U_{\alpha j}^* U_{\beta j} \sin^2 \left(\frac{1.27 \Delta m_{ij}^2 L}{E} \right), \quad (2)$$

where $\Delta m_{ij}^2 = m_j^2 - m_i^2$, α and β are flavor-state indices (e, μ, τ), and i and j are mass-state indices (1, 2, 3 in the three-neutrino case, though Eq. 2 holds for n -neutrino oscillations). Although in general there will be mixing among all three flavors of neutrinos, if the mass scales are quite different ($m_3 \gg m_2 \gg m_1$), then the oscillation phenomena tend to decouple and the two neutrino mixing model is a good approximation in limited regions.

Three different Δm^2 parameters appear in Eq. 2; however, only two are independent since the two small Δm^2 parameters must sum to the largest. If we consider the oscillation data measured at $> 5\sigma$ [1–16], then two Δm^2 ranges, $7 \times 10^{-5} \text{ eV}^2$ (solar) and $3 \times 10^{-3} \text{ eV}^2$ (atmospheric) are already defined. These constrain the third Δm^2 , so that oscillation results at 1 eV^2 , such as those discussed in this paper, cannot be accommodated within a three-neutrino model.

2.3 (3+N) Oscillation Formalism

The sterile neutrino oscillation formalism followed in this paper assumes up to three additional neutrino mass eigenstates, beyond the established three SM neutrino species. We know, from solar and atmospheric oscillation observations, that three of the mass states must be mostly active. Experimental hints point toward the existence of additional mass states that are mostly sterile, in the range of $\Delta m^2 = 0.01 - 100 \text{ eV}^2$.

Introducing extra mass states results in a large number of extra parameters in the model. Approximation is required to allow for efficient exploration of the available parameters. To this end, in our model we assume that the three lowest states, ν_1 , ν_2 , and ν_3 , that are the mostly active states accounting for the solar and atmospheric observations, have masses so small as to be effectively degenerate with masses of zero. This is commonly called the “short baseline approximation” and it reduces the fit to two-, three-, and four-neutrino-mass oscillation models, corresponding to (3+1), (3+2), and (3+3), respectively.

The active (e, μ, τ) content of the N additional mass eigenstates is assumed to be small; specifically, the $U_{\alpha i}$ elements of the extended $(3+N) \times (3+N)$ mixing matrix for $i = 4 - 6$ and $\alpha = e, \mu, \tau$, are restricted to values $|U_{\alpha i}| \leq 0.5$, while the following constraints are applied by way of unitarity:

$$\sum_{\alpha=e,\mu,\tau} |U_{\alpha i}|^2 \leq 0.3, \quad (3)$$

for each $i = 4 - 6$, and

$$\sum_{i=4-6} |U_{\alpha i}|^2 \leq 0.3, \quad (4)$$

for each $\alpha = e, \mu, \tau$. In our fits, since the SBL experiments considered have no ν_τ sensitivity, we explicitly assume $|U_{\tau i}| = 0$. The above restrictions therefore apply only for $\alpha = e, \mu$, and are consistent

with solar and atmospheric neutrino experiments, which indicate that there can only be a small electron and muon flavor content in the fourth, fifth and sixth mass eigenstates [23].

In this formalism, the probabilities for $\nu_\alpha \rightarrow \nu_\beta$ oscillations can be deduced from the following equation:

$$P(\nu_\alpha \rightarrow \nu_\beta) = \delta_{\alpha\beta} - \sum_{j < i} (4\text{Re}\{U_{\beta i}U_{\alpha i}^*U_{\beta j}^*U_{\alpha j}\} \sin^2(1.27\Delta m_{ij}^2 L/E) - 2\text{Im}\{U_{\beta i}U_{\alpha i}^*U_{\beta j}^*U_{\alpha j}\} \sin(2.53\Delta m_{ij}^2 L/E)) , \quad (5)$$

where $\Delta m_{ij}^2 = m_i^2 - m_j^2$ is in eV^2 , L is in m, and E is in MeV. This formalism conserves CPT, but does not necessarily conserve CP.

To be explicit, for the (3+3) scenario, the mixing formalism is extended in the following way:

$$\begin{pmatrix} \nu_e \\ \nu_\mu \\ \nu_\tau \\ \nu_{s1} \\ \nu_{s2} \\ \nu_{s3} \end{pmatrix} = \begin{pmatrix} U_{e1} & U_{e2} & U_{e3} & U_{e4} & U_{e5} & U_{e6} \\ U_{\mu1} & U_{\mu2} & U_{\mu3} & U_{\mu4} & U_{\mu5} & U_{\mu6} \\ U_{\tau1} & U_{\tau2} & U_{\tau3} & U_{\tau4} & U_{\tau5} & U_{\tau6} \\ U_{s11} & U_{s12} & U_{s13} & U_{s14} & U_{s15} & U_{s16} \\ U_{s21} & U_{s22} & U_{s23} & U_{s24} & U_{s25} & U_{s26} \\ U_{s31} & U_{s32} & U_{s33} & U_{s34} & U_{s35} & U_{s36} \end{pmatrix} \begin{pmatrix} \nu_1 \\ \nu_2 \\ \nu_3 \\ \nu_4 \\ \nu_5 \\ \nu_6 \end{pmatrix}$$

The SBL approximation states that $\nu_1 \approx \nu_2 \approx \nu_3 \equiv 0$. With this assumption and for the case of the (3+3) scenario, the appearance ($\alpha \neq \beta$) oscillation probability can be re-written as:

$$\begin{aligned} P(\nu_\alpha \rightarrow \nu_\beta) \simeq & -4|U_{\alpha 5}||U_{\beta 5}||U_{\alpha 4}||U_{\beta 4}| \cos \phi_{54} \sin^2(1.27\Delta m_{54}^2 L/E) \\ & -4|U_{\alpha 6}||U_{\beta 6}||U_{\alpha 4}||U_{\beta 4}| \cos \phi_{64} \sin^2(1.27\Delta m_{64}^2 L/E) \\ & -4|U_{\alpha 5}||U_{\beta 5}||U_{\alpha 6}||U_{\beta 6}| \cos \phi_{65} \sin^2(1.27\Delta m_{65}^2 L/E) \\ & +4(|U_{\alpha 4}||U_{\beta 4}| + |U_{\alpha 5}||U_{\beta 5}| \cos \phi_{54} + |U_{\alpha 6}||U_{\beta 6}| \cos \phi_{64})|U_{\alpha 4}||U_{\beta 4}| \sin^2(1.27\Delta m_{41}^2 L/E) \\ & +4(|U_{\alpha 4}||U_{\beta 4}| \cos \phi_{54} + |U_{\alpha 5}||U_{\beta 5}| + |U_{\alpha 6}||U_{\beta 6}| \cos \phi_{65})|U_{\alpha 5}||U_{\beta 5}| \sin^2(1.27\Delta m_{51}^2 L/E) \\ & +4(|U_{\alpha 4}||U_{\beta 4}| \cos \phi_{64} + |U_{\alpha 5}||U_{\beta 5}| \cos \phi_{65} + |U_{\alpha 6}||U_{\beta 6}|)|U_{\alpha 6}||U_{\beta 6}| \sin^2(1.27\Delta m_{61}^2 L/E) \\ & +2|U_{\beta 5}||U_{\alpha 5}||U_{\beta 4}||U_{\alpha 4}| \sin \phi_{54} \sin(2.53\Delta m_{54}^2 L/E) \\ & +2|U_{\beta 6}||U_{\alpha 6}||U_{\beta 4}||U_{\alpha 4}| \sin \phi_{64} \sin(2.53\Delta m_{64}^2 L/E) \\ & +2|U_{\beta 6}||U_{\alpha 6}||U_{\beta 5}||U_{\alpha 5}| \sin \phi_{65} \sin(2.53\Delta m_{65}^2 L/E) \\ & +2(|U_{\alpha 5}||U_{\beta 5}| \sin \phi_{54} + |U_{\alpha 6}||U_{\beta 6}| \sin \phi_{64})|U_{\alpha 4}||U_{\beta 4}| \sin(2.53\Delta m_{41}^2 L/E) \\ & +2(-|U_{\alpha 4}||U_{\beta 4}| \sin \phi_{54} + |U_{\alpha 6}||U_{\beta 6}| \sin \phi_{65})|U_{\alpha 5}||U_{\beta 5}| \sin(2.53\Delta m_{51}^2 L/E) \\ & +2(-|U_{\alpha 4}||U_{\beta 4}| \sin \phi_{64} - |U_{\alpha 5}||U_{\beta 5}| \sin \phi_{65})|U_{\alpha 6}||U_{\beta 6}| \sin(2.53\Delta m_{61}^2 L/E) . \end{aligned} \quad (6)$$

CP violation appears in Eq. 6 in the form of the three phases, defined by

$$\phi_{54} = \arg(U_{e5}U_{\mu 5}^*U_{e4}^*U_{\mu 4}) , \quad (7)$$

$$\phi_{64} = \arg(U_{e6}U_{\mu 6}^*U_{e4}^*U_{\mu 4}) , \quad (8)$$

and

$$\phi_{65} = \arg(U_{e6}U_{\mu 6}^*U_{e5}^*U_{\mu 5}) . \quad (9)$$

In each case, $\nu \rightarrow \bar{\nu}$ implies $\phi \rightarrow -\phi$. In the case of disappearance ($\alpha \equiv \beta$), the survival probability can be re-written as:

$$\begin{aligned}
P(\nu_\alpha \rightarrow \nu_\alpha) \simeq & 1 - 4|U_{\alpha 4}|^2|U_{\alpha 5}|^2 \sin^2(1.27\Delta m_{54}^2 L/E) \\
& - 4|U_{\alpha 4}|^2|U_{\alpha 6}|^2 \sin^2(1.27\Delta m_{64}^2 L/E) - 4|U_{\alpha 5}|^2|U_{\alpha 6}|^2 \sin^2(1.27\Delta m_{65}^2 L/E) \\
& - 4(1 - |U_{\alpha 4}|^2 - |U_{\alpha 5}|^2 - |U_{\alpha 6}|^2)(|U_{\alpha 4}|^2 \sin^2(1.27\Delta m_{41}^2 L/E) \\
& + |U_{\alpha 5}|^2 \sin^2(1.27\Delta m_{51}^2 L/E) + |U_{\alpha 6}|^2 \sin^2(1.27\Delta m_{61}^2 L/E)) .
\end{aligned} \tag{10}$$

This formula has no ϕ_{ij} dependencies because CP violation only affects appearance.

We have discussed the formulas for (3+1) and (3+2) oscillations that arise from Eq. 5 in previous papers [20–22]. To reduce to a (3+2) model, the parameters Δm_{61}^2 , $|U_{e6}|$, $|U_{\mu 6}|$, ϕ_{64} and ϕ_{65} are explicitly set to zero, in which case we have the following appearance and disappearance formulas for a (3+2) model:

$$\begin{aligned}
P(\nu_\alpha \rightarrow \nu_\beta) \simeq & -4|U_{\alpha 5}||U_{\beta 5}||U_{\alpha 4}||U_{\beta 4}| \cos \phi_{54} \sin^2(1.27\Delta m_{54}^2 L/E) \\
& + 4(|U_{\alpha 4}||U_{\beta 4}| + |U_{\alpha 5}||U_{\beta 5}| \cos \phi_{54})|U_{\alpha 4}||U_{\beta 4}| \sin^2(1.27\Delta m_{41}^2 L/E) \\
& + 4(|U_{\alpha 4}||U_{\beta 4}| \cos \phi_{54} + |U_{\alpha 5}||U_{\beta 5}|)|U_{\alpha 5}||U_{\beta 5}| \sin^2(1.27\Delta m_{51}^2 L/E) \\
& + 2|U_{\beta 5}||U_{\alpha 5}||U_{\beta 4}||U_{\alpha 4}| \sin \phi_{54} \sin(2.53\Delta m_{54}^2 L/E) \\
& + 2(|U_{\alpha 5}||U_{\beta 5}| \sin \phi_{54})|U_{\alpha 4}||U_{\beta 4}| \sin(2.53\Delta m_{41}^2 L/E) \\
& + 2(-|U_{\alpha 4}||U_{\beta 4}| \sin \phi_{54})|U_{\alpha 5}||U_{\beta 5}| \sin(2.53\Delta m_{51}^2 L/E) ,
\end{aligned} \tag{11}$$

and

$$\begin{aligned}
P(\nu_\alpha \rightarrow \nu_\alpha) \simeq & 1 - 4|U_{\alpha 4}|^2|U_{\alpha 5}|^2 \sin^2(1.27\Delta m_{54}^2 L/E) \\
& - 4(1 - |U_{\alpha 4}|^2 - |U_{\alpha 5}|^2)(|U_{\alpha 4}|^2 \sin^2(1.27\Delta m_{41}^2 L/E) \\
& + |U_{\alpha 5}|^2 \sin^2(1.27\Delta m_{51}^2 L/E)) .
\end{aligned} \tag{12}$$

For a (3+1) model, Δm_{61}^2 , Δm_{51}^2 , $|U_{e6}|$, $|U_{\mu 6}|$, $|U_{e5}|$, $|U_{\mu 5}|$, ϕ_{64} , ϕ_{65} and ϕ_{54} should be set to zero. This further simplifies the oscillation probabilities, and one recovers the familiar two-neutrino appearance and disappearance probabilities. The appearance and disappearance formulas for a (3+1) model are then given by:

$$P(\nu_\alpha \rightarrow \nu_\beta) \simeq 4|U_{\alpha 4}|^2|U_{\beta 4}|^2 \sin^2(1.27\Delta m_{41}^2 L/E) , \tag{13}$$

and

$$P(\nu_\alpha \rightarrow \nu_\alpha) \simeq 1 - 4(1 - |U_{\alpha 4}|^2)|U_{\alpha 4}|^2 \sin^2(1.27\Delta m_{41}^2 L/E) . \tag{14}$$

In principle, the probability for neutrino oscillation is modified in the presence of matter. “Matter effects” arise because the electron neutrino flavor experiences both Charged Current (CC) and Neutral Current (NC) elastic forward-scattering with electrons as it propagates through matter, while the ν_μ and ν_τ experience only NC forward-scattering. The sterile component experiences no forward-scattering. In practice, SM-inspired matter effects are very small given the short baselines of the experiments, and so we do not consider them further here. Beyond-SM matter effects are beyond the scope of this article, but are considered in Ref. [32].

3 Experimental Data Sets

This section provides an overview of the various types of past and existing neutrino sources and detectors used in SBL experiments. After introducing the experimental concepts, the specific experimental data sets used in this analysis are discussed.

The data fall into two overall types: disappearance, where the active flavor is assumed to have oscillated into a sterile neutrino and/or another flavor which is kinematically not allowed to interact or leaves no detectable signature; and appearance, where the transition is between active flavors, but with mass splittings corresponding to the mostly-sterile states. Appearance and disappearance are natural divisions for testing the compatibility of data sets, as can be seen clearly from Eqs. 13 and 14. If $|U_{\alpha 4}|^2$ and $|U_{\beta 4}|^2$ are shown to be small, then the effective mixing angle for appearance, $4|U_{\alpha 4}|^2|U_{\beta 4}|^2$, cannot be large. This constraint that the disappearance experiments place on appearance experiments extends to (3+2) and (3+3) models also.

CPT conservation, which is assumed in the analysis, demands that neutrino and antineutrino disappearance probabilities are the same. To test this, we divide the data into antineutrino and neutrino sets and fit each set separately. If CP violation is already allowed in the oscillation formalism, then any incompatibility found between respective neutrino and antineutrino fits could imply effective CPT violation, as discussed in Ref. [22].

Figures 1, 2, and 3 provide summaries of the data sets, showing the constraints they provide in a simple two-neutrino oscillation model, which is functionally equivalent to the (3+1) scenario. Figure 1 shows the muon-to-electron flavor data sets in neutrino and antineutrino mode at 95% confidence level (CL). Figures 2 and 3 show results for ν_μ and $\bar{\nu}_\mu$, and ν_e and $\bar{\nu}_e$ disappearance, respectively.

3.1 Sources and Detectors Used in Short Baseline Neutrino Experiments

Before considering the data sets in detail, we provide an overview of how SBL experiments are typically designed.

3.1.1 Sources of Neutrinos for Short Baseline Experiments

The neutrino sources used in SBL experiments range in energy from a few MeV to hundreds of GeV and include man-made radioactive sources, reactors, and accelerator-produced beams. While the higher energy accelerator sources are mixtures of different neutrino flavors, the < 10 MeV sources rely on beta decay and are thus pure electron neutrino flavor.

At the low energy end of the spectrum, the rate of electron neutrino interactions from the beta decay of the ~ 1 MCi sources ^{51}Cr (half-life: 28 days) and ^{37}Ar (half-life: 35 days) have been studied. These sources were originally produced for the low energy (~ 1 MeV) calibration of solar neutrino detectors [33, 34] but have proven themselves interesting as a probe of electron neutrino disappearance.

Moving up in energy by a few MeV, nuclear reactors are powerful sources of ~ 2 -8 MeV $\bar{\nu}_e$ through the β^+ -decaying elements produced primarily in the decay chains of ^{235}U , ^{239}Pu , ^{238}U and ^{241}Pu . While these four isotopes are the progenitors of most of the reactor flux, modern reactor simulations include all fission sources [35]. Reactor simulations convolute predictions of fission rates over time with neutrino production per fission. Recently, a reanalysis of the production cross section per fission [23, 36, 37] has led to an increase in the predicted reactor flux. As their energy is too low for an appearance search (the neutrino energy is below the muon production kinematic threshold), reactor

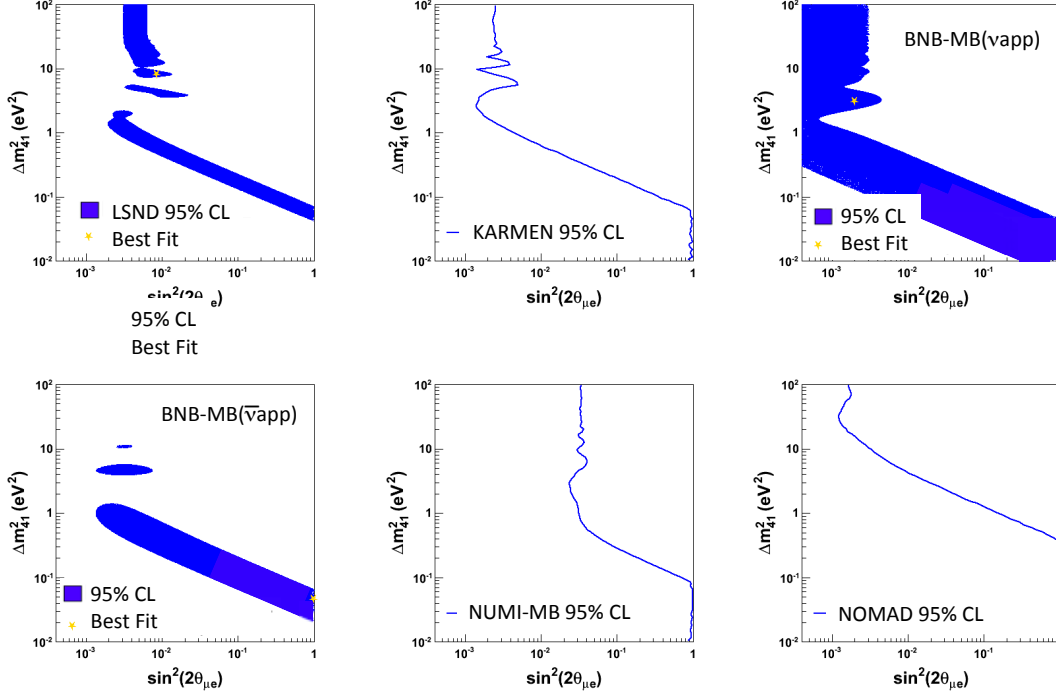


Figure 1: Summary of $\bar{\nu}_\mu \rightarrow \bar{\nu}_e$ and $\nu_\mu \rightarrow \nu_e$ results, shown at 95% CL. Top row: LSND, KARMEN, BNB-MB(ν_{app}); Bottom row: BNB-MB($\bar{\nu}_{app}$), NuMI-MB(ν_{app}), NOMAD. See Sec. 3.2 for details and references.

source neutrinos can only be used for $\bar{\nu}_e$ disappearance searches, where the neutrinos are detected using CC interactions with an outgoing e^+ .

The lowest neutrino energy (up to 53 MeV) accelerator sources used in existing SBL experiments are based on pion- and muon-decay-at-rest (DAR). The neutrino flux comes from the stopped pion decay chain: $\pi^+ \rightarrow \mu^+ \nu_\mu$ and $\mu^+ \rightarrow e^+ \bar{\nu}_\mu \nu_e$. Pions are produced in interactions of accelerator protons with a, typically, graphite or water target. The contribution from the decay chain $\pi^- \rightarrow \mu^- \bar{\nu}_\mu$ is suppressed by designing the target such that the π^- mesons are captured with high probability. The result is a source which has a well understood neutrino flavor content and energy distribution, with a minimal ($< 10^{-3}$) $\bar{\nu}_e$ content [38, 39]. This last point is important as $\bar{\nu}_\mu \rightarrow \bar{\nu}_e$ is the dominant channel used for oscillation searches by DAR sources.

In a conventional high energy (from ~ 100 MeV to hundreds of GeV) accelerator-based neutrino beam, protons impinge on a target (beryllium and carbon are typical) to produce secondary mesons. The boosted mesons enter and subsequently decay inside of a long, often evacuated pipe. Neutrinos are primarily produced by π^+ and π^- decay in flight (DIF). Pion sign selection, via a large magnet placed directly in the beamlines before the decay pipe, allows for nearly pure neutrino or antineutrino running, with only a few percent “wrong sign” neutrino flux content in the case of neutrino running, and $\sim 15\%$ [40] in the case of antineutrino running. These beams are generally produced by protons at

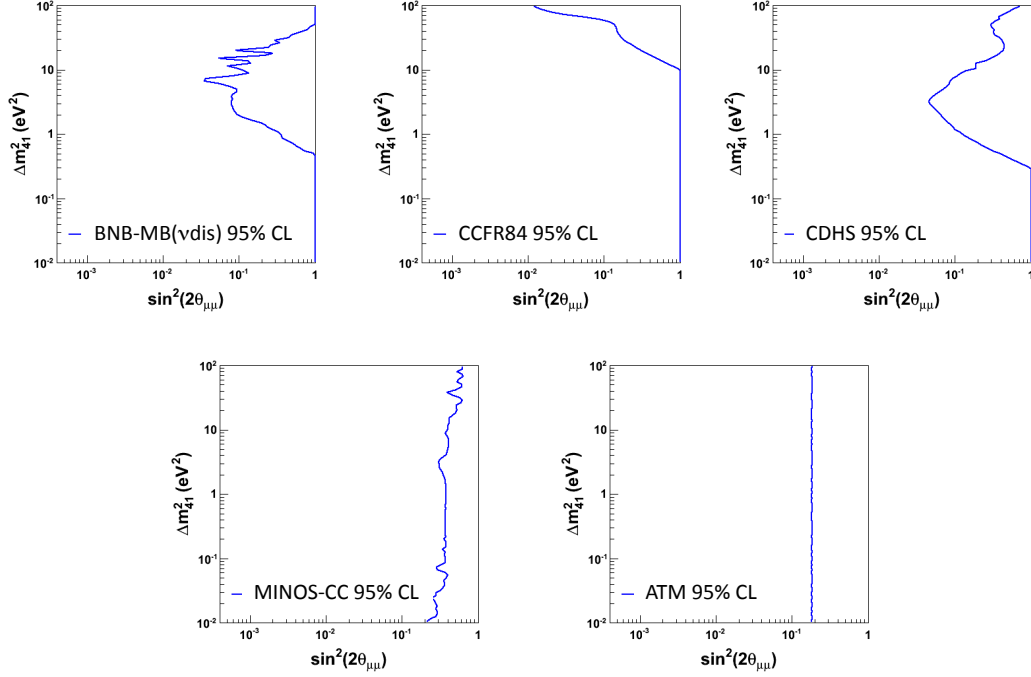


Figure 2: Summary of $\bar{\nu}_\mu \rightarrow \bar{\nu}_\mu$ and $\nu_\mu \rightarrow \nu_\mu$ results, shown at 95% CL. Top row: BNB-MB(ν_{dis}), CCFR84, CDHS; Bottom row: MINOS-CC, ATM. See Sec. 3.2 for details and references.

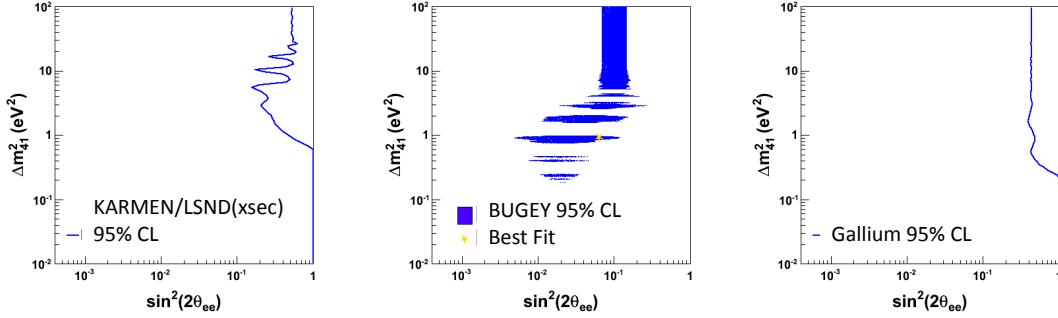


Figure 3: Summary of $\bar{\nu}_e \rightarrow \bar{\nu}_e$ and $\nu_e \rightarrow \nu_e$ results, shown at 95% CL. From left: KARMEN/LSND(xsec), Bugey, and Gallium. See Sec. 3.2 for details and references.

8 GeV and above. At these energies, in addition to pion production, kaon production contributes to the flux of both muon and electron neutrino flavor. There is often a substantial muon DIF content as well, contributing both $\nu_e/\bar{\nu}_e$ and $\bar{\nu}_\mu/\nu_\mu$ to the beam. The result of the kaon and muon secondary content is that, while the neutrinos are predominantly muon-flavored, the beam will always have some intrinsic electron-flavor neutrino content, usually at the several percent level. Accelerator-based beams are predominantly used for $\nu_\mu \rightarrow \nu_e$ and $\bar{\nu}_\mu \rightarrow \bar{\nu}_e$ appearance searches, as well as ν_μ and $\bar{\nu}_\mu$ disappearance searches. An excellent review of methods in producing accelerator-based neutrino beams can be found in Ref. [41].

In contrast to lower-energy neutrino sources (DAR, reactor, and isotope sources), high energy accelerator-based neutrino sources are subject to significant energy dependent neutrino flux uncertainties, often at the level of 10-15%, due to in-target meson production uncertainties. These uncertainties can affect the energy distribution, flavor content, and absolute normalization of a neutrino beam. Typically, meson production systematics are constrained with dedicated measurements by experiments such as HARP [42] and MIPP [43], which use replicated targets (geometry and material) and a wide range of proton beam energies to study meson production cross sections and kinematics directly. Alternatively, experiments can employ a two-detector design for comparing near-to-far event rate in energy to effectively reduce these systematics. However, due to the short baselines employed for studying sterile neutrino oscillations, a two-detector search is often impractical. *In-situ* measurements in single detector experiments can exploit flux (times cross section) correlations among different beam components and energies to reduce flux uncertainties, as has been done in the case of the MiniBooNE ν_e and $\bar{\nu}_e$ appearance searches described below.

3.1.2 Short Baseline Neutrino Detectors

Because low energy neutrino interaction cross sections are very small, the options for SBL detectors are typically limited to designs which can be constructed on a massive scale. There are several generic neutrino detection methods in use today: unsegmented scintillator detectors, unsegmented Cerenkov detectors, segmented scintillator-and-iron calorimeters, and segmented trackers.

Neutrino oscillation experiments usually require sensitivity to charged current (CC) neutrino interactions, whereby one can definitively identify the flavor of the interacting neutrino by the presence of a charged lepton in the final state. However, in the case of sterile neutrino oscillation searches, neutral current (NC) interactions can also provide useful information, as they are directly sensitive to the sterile flavor content of the neutrino mass eigenstate, $|U_{si}|^2 = 1 - |U_{ei}|^2 - |U_{\mu i}|^2 - |U_{\tau i}|^2$.

Unsegmented scintillator detectors are typically used for few-MeV-scale SBL experiments, which require efficient electron neutrino identification and reconstruction. These detectors consist of large tanks of oil-based (C_nH_{2n}) liquid scintillator surrounded by phototubes. The free protons in the oil provide a target for the inverse beta decay interaction, $\bar{\nu}_e p \rightarrow e^+ n$. The reaction threshold for this interaction is 1.8 MeV due to the mass difference between the proton and neutron and the mass of the positron. The scintillation light from the e^+ , as well as light from the Compton scattering of the 0.511 MeV annihilation photons provides an initial (“prompt”) signal. This is followed by n capture on hydrogen and a 2.2 MeV flash of light, as the resulting γ Compton-scatters in the scintillator. This coincidence sequence in time (positron followed by neutron capture) provides a clean, mostly background-free interaction signature. Experiments often dope the liquid scintillator using an element with a high neutron capture cross section for improved event identification efficiency.

The CC interaction with the carbon in the oil (which produces either nitrogen or boron depending

on whether the scatterer is a neutrino or antineutrino) has a significantly higher energy threshold than the free proton target scattering process. The CC quasielastic interaction $\nu_e + C \rightarrow e^- + N$ has an energy threshold of 13.4 MeV, which arises from the carbon-nitrogen mass difference and the mass of the electron. In the case of both reactor and radioactive decay sources, the flux cuts off below this energy threshold. However, neutrinos from DAR sources are at sufficiently high energy to produce these carbon scatters.

Unsegmented Cerenkov detectors make use of a target which is a large volume of clear medium (undoped oil or water are typical) surrounded by or interspersed with phototubes. Undoped oil has a larger refractive index, leading to a larger Cerenkov opening angle. Water is the only affordable medium once the detector size surpasses a few kilotons. In this paper, the only unsegmented Cerenkov detector that is considered is the 450 ton oil-based MiniBooNE detector. In such a detector, a track will project a ring with a sharp inner and outer edge onto the phototubes. Consider an electron produced in a ν_e CC quasielastic interaction. As the electron is low mass, it will multiple scatter and easily bremsstrahlung, smearing the light projected on the tubes and producing a “fuzzy” ring. A muon produced by a CC quasielastic ν_μ interaction ($\nu_\mu n \rightarrow \mu^- p$) is heavier and will thus produce a sharper outer edge to the ring. For the same visible energy, the track will also extend farther, filling the interior of the ring, and perhaps exit the tank. If the muon stops within the tank and subsequently decays, the resulting electron provides an added tag for particle identification. In the case of the μ^- , 18% will capture in water, and thus have no electron tag, while only 8% will capture in the oil.

Scintillator and iron calorimeters provide an affordable detection technique for ~ 1 GeV and higher ν_μ interactions. At these energies, multiple hadrons may be produced at the interaction vertex and will be observed as hadronic showers. In these devices, the iron provides the target, while the scintillator provides information on energy deposition per unit length. This information allows separation between the hadronic shower, which occurs in both NC and CC events, and the minimum ionizing track of an outgoing muon, which occurs in CC events. Transverse information can be obtained if segmented scintillator strips are used, or if drift chambers are interspersed. The light from scintillator strips is transported to tubes by wavelength-shifting fibers. Information in the transverse plane improves separation of electromagnetic and hadronic showers. The iron can be magnetized to allow separation of neutrino and antineutrino events based on the charge of the outgoing lepton.

To address the problem of running at ~ 1 GeV, where hadron track reconstruction is desirable, highly segmented tracking designs have been developed. The best resolution comes from stacks of wire chambers, where the material enclosing the gas provides the target. However, a more practical alternative has been stacks of thin, extruded scintillator bars that are read out using wavelength shifting fibers.

3.2 Data Used in The Sterile Neutrino Fits

There are many SBL data sets that can be included in this analysis. In this work, we have substantially expanded the number of data sets used beyond those in our past papers [20–22]. We identify and discuss new and updated data sets, as well as provide information on those used in past fits, below. The fit technique is described in Sec. 4.2.

3.2.1 Experimental Results from Decay at Rest Studies

In past sterile neutrino studies [20–22], we have included the LSND and KARMEN appearance results described below. Since that work, a new study that constrains $\bar{\nu}_e$ disappearance from the relative LSND-to-KARMEN cross section measurements was published [44]. This new data set is included in this analysis.

LSND Appearance:

LSND was a DAR experiment that ran in the 1990’s, searching for $\bar{\nu}_\mu \rightarrow \bar{\nu}_e$. The beam was produced using 800 MeV protons on target from the LAMPF accelerator at Los Alamos National Laboratory, where a 1 mA beam of protons impinged on a water target. The center of the 8.75 m long, nearly cylindrical detector was located at 29.8 m from the target, at an angle of 12° from the proton beam direction. This was an unsegmented detector with a fiducial mass of 167 tons of oil (CH_2), lightly doped with b-PBD scintillator. The intrinsic $\bar{\nu}_e$ content of the beam was 8×10^{-4} of the $\bar{\nu}_\mu$ content. The experiment observed a $\bar{\nu}_e$ excess of $87.9 \pm 22.4 \pm 6.0$ events above background, which was interpreted as oscillations with a probability of $(0.264 \pm 0.067 \pm 0.045)\%$. Details are available in Ref. [17].

This data set is referred to as **LSND** in the analysis below and indicates a signal at 95% CL shown in Fig. 1. This data covers energies between 20 and 53 MeV and contributes 5 energy bins to the global fit. Statistical errors are taken into account by using a log-likelihood χ^2 definition in the fit, while systematic errors on the background prediction are not included because these are small relative to the statistical error. Energy and baseline smearing are taken into account by averaging the oscillation probability over the energy bin width and over the neutrino flight path uncertainty.

KARMEN Appearance:

KARMEN was another DAR experiment searching for $\bar{\nu}_\mu \rightarrow \bar{\nu}_e$. KARMEN ran at the ISIS facility at Rutherford Laboratory, with 200 μA of protons impinging on a copper, tantalum, or uranium target. The neutrino detector was located at an angle of 100° with respect to the targeting protons to reduce background from π^- DIF. The resulting intrinsic $\bar{\nu}_e$ content was 6.4×10^{-4} of the $\bar{\nu}_\mu$ content.

The center of the approximately cubic, segmented scintillator detector was located at 17.7 m. Thus, this detector was 60% of the distance from the source compared to LSND. The liquid scintillator target volume was 56 m^3 and consisted of 512 optically independent modules ($17.4 \text{ cm} \times 17.8 \text{ cm} \times 353 \text{ cm}$) wrapped in gadolinium-doped paper. KARMEN saw no signal and set a limit on appearance. More details are available in Ref. [45].

This data set is referred to as **KARMEN** in the analysis below and indicates a limit at 95% CL, as shown in Fig. 1. This data set contributes 9 energy bins, in the range 16 to 50 MeV. As in the case of LSND, statistical errors are taken into account by using a log-likelihood χ^2 definition in the fit, while systematic errors on the background prediction are not included. Energy and baseline smearing are taken into account by averaging the $\sin^2(1.27\Delta m^2 L/E)$ and $\sin(2.53\Delta m^2 L/E)$ term contributions in the total signal prediction over energy bin widths. The limit which is shown here is determined using a $\Delta\chi^2$ -based raster scan, as discussed in Sec 4.2

LSND and KARMEN Cross Section Measurements:

Along with the oscillation searches, LSND and KARMEN measured $\nu_e + {}^{12}\text{C} \rightarrow {}^{12}\text{N}_{gs} + e^-$ scattering. In this two-body interaction, with a Q -value of 17.3 MeV, the neutrino energy can be reconstructed by measuring the outgoing visible energy of the electron. The ${}^{12}\text{N}$ ground state is identified by the subsequent β decay, ${}^{12}\text{N}_{gs} \rightarrow {}^{12}\text{C} + e^+ + \nu_e$, which has a Q -value of 16.3 MeV and a lifetime of 15.9 ms.

The cross section is measured by both experiments under the assumption that the ν_e flux has not oscillated, leading to disappearance. The excellent agreement between the two results, as a function of energy, allows a limit to be placed on ν_e oscillations. The energy dependence of the cross section, as well as the normalization, are well predicted and both constraints are used in the analysis [44].

This data set is referred to as **KARMEN/LSND(xsec)** in the analysis below, and indicates a limit at 95% CL as shown in Fig. 3. A total of six (for KARMEN) plus five (for LSND) bins are used in the fit, which extend approximately from 28-50 MeV in the case of KARMEN and from 38-50 MeV in the case of LSND. In calculating the oscillation probability, the signal is averaged across the lengths of the detectors. The experiments have correlated systematics arising from the flux normalization due to a shared underlying analysis for pion production in DAR experiments. This is addressed through application of pull-terms as described in Ref. [44].

3.2.2 The MiniBooNE Experimental Results

The MiniBooNE experiment provides multiple results from a single detector. This oil-based 450 t fiducial volume Cerenkov detector was exposed to two conventional beams, the Booster Neutrino Beam (BNB) and the off-axis NuMI beam. The primary goal of MiniBooNE was to search for $\nu_\mu \rightarrow \nu_e$ and $\bar{\nu}_\mu \rightarrow \bar{\nu}_e$ appearance, using the BNB, which provides sensitivity to $\Delta m^2 \sim 0.1 - 10 \text{ eV}^2$ oscillations. The NuMI beam also provides some sensitivity to $\nu_\mu \rightarrow \nu_e$ appearance at a similar Δm^2 . In addition to the appearance searches, MiniBooNE also looked for ν_μ and $\bar{\nu}_\mu$ disappearance using the BNB.

The MiniBooNE data sets included in our analysis have increased throughout the period that our group has been performing fits. Ref. [21] used a Monte Carlo prediction for neutrinos and antineutrinos to estimate MiniBooNE's sensitivity to sterile neutrinos. The full BNB neutrino and first published BNB antineutrino data sets from MiniBooNE form the experimental constraints in Ref. [22]. Here, we have updated to include the full BNB antineutrino data sets. A further update has been to employ a log-likelihood method for the BNB neutrino and antineutrino data sets from [46], as this was recently adopted by the MiniBooNE collaboration [47]. We also use the updated constraints on electron neutrino flux from kaons [46]. A partial data set from NuMI data taking was presented in Ref. [22] and has not been updated, as the result was already systematics limited. In this analysis we also introduce the MiniBooNE disappearance search [48].

In our fits to MiniBooNE appearance data, when drawing allowed regions and calculating compatibilities, which make use of $\Delta\chi^2$'s and not absolute χ^2 's, we use MiniBooNE's log-likelihood χ^2 definition, summing over both ν_e and ν_μ bins, as described in [47]. For consistency, the absolute MiniBooNE BNB ν_e and $\bar{\nu}_e$ appearance χ^2 values quoted in our paper also correspond to the same definition, i.e. fitting to both ν_e and ν_μ spectra; therefore, they differ from the ones published by MiniBooNE in [46], which are obtained by fitting only to *a priori* constrained ν_e distributions. Note that the two definitions should yield consistent allowed regions and compatibility results.

The Booster Beam Appearance Search in Neutrino Running Mode:

The BNB flux composition in neutrino mode consists of $> 90\%$ ν_μ , 6% $\bar{\nu}_\mu$, and 0.06% ν_e and $\bar{\nu}_e$ combined [40]. In the MiniBooNE BNB search for ν_e appearance, the ν_e and $\bar{\nu}_e$ signal was normalized to the ν_μ and $\bar{\nu}_\mu$ CC quasielastic events observed in the detector, which peaked at 700 MeV.

The global fits presented here use the full statistics of the MiniBooNE $\nu_\mu \rightarrow \nu_e$ data set, representing 6.46×10^{20} protons on target. In this data set, MiniBooNE has observed an excess of events at $200 - 1250$ MeV, corresponding to 161.9 ± 49.0 electron-like events [46]. The data set is referred to as **BNB-MB(ν_{app})** in the analysis below.

We include the BNB-MB(ν_{app}) data set in our fits in the form of the full ν_e CC reconstructed energy distribution, in 11 bins in energy from 200 to 3000 MeV, fit simultaneously with the full ν_μ CC energy distribution, in 8 bins in energy up to 1900 MeV. We account for statistical and systematic uncertainties in each sample, as well as systematic correlations (from flux and cross section) among the ν_e signal and background and ν_μ background distributions. The systematic correlations are provided in the form of a full 19-bin \times 19-bin fractional covariance matrix. By fitting the ν_e and ν_μ spectra simultaneously, we are able to exploit the high-statistics ν_μ CC sample as a constraint on background and signal event rates, by assuming no significant ν_μ disappearance. For further information, see Ref. [18].

The data set results in a signal at 95% CL, as shown in Fig. 1. This has changed slightly from our past analysis [22] now that we are using updated constraints on intrinsic electron neutrinos from kaons and the log-likelihood method, but is in agreement with the equivalent analysis from the MiniBooNE Collaboration [46].

The Booster Beam Appearance Search in Antineutrino Running Mode:

The BNB flux composition in antineutrino mode consists of 83% $\bar{\nu}_\mu$, 0.6% ν_e combined and $\bar{\nu}_e$, and a significantly larger wrong-sign composition than in neutrino mode, of 16% ν_μ . As in the BNB ν_e appearance search, the electron flavor signal was normalized to the muon-flavor CC quasielastic events observed in the detector, which peaked at 500 MeV.

The global fits presented here use the full statistics of the MiniBooNE $\bar{\nu}_\mu$ data set, representing 11.27×10^{20} protons on target. In this data set, MiniBooNE has observed an excess of events at $200 - 1250$ MeV, corresponding to 78.4 ± 30.8 electron-like events. The data set is referred to as **BNB-MB($\bar{\nu}_{\text{app}}$)** in the analysis below.

As in neutrino mode, we fit the full $\bar{\nu}_e$ CC energy distribution, in 11 bins in energy from 200 to 3000 MeV, simultaneously with the full $\bar{\nu}_\mu$ CC energy distribution, in 8 bins in energy up to 1900 MeV. The wrong-sign contamination in the beam (ν_μ) is assumed to not contribute to any oscillations; only $\bar{\nu}_\mu \rightarrow \bar{\nu}_e$ oscillations are assumed for this data set. We account for statistical and systematic uncertainties in each sample, as well as systematic correlations among the $\bar{\nu}_e$ and $\bar{\nu}_\mu$ distributions in the form of a full 19-bin \times 19-bin fractional covariance matrix in each fit. For further information, see Ref. [18].

The data set results in a signal at 95% CL, as shown in Fig. 1.

The NuMI Beam Appearance Search:

The MiniBooNE detector is also exposed to the NuMI neutrino beam, arising from a 120 GeV proton beam impinging on a carbon target. This beam is nominally used for the MINOS long baseline neutrino oscillation experiment. NuMI events arrive out-of-time with the BNB-produced events. This 200 MeV to 3 GeV neutrino energy source is dominated by kaon decays near the NuMI target, which is 110 mrad off-axis and located 745 m upstream of the MiniBooNE detector. The beam consists of 81% ν_μ , 13% $\bar{\nu}_\mu$, 5% ν_e and 1% $\bar{\nu}_e$. For more information on this data see Ref. [49].

This data set is referred to as **NuMI-MB(ν app)** in the analysis below. As seen in Fig. 1, the data set provides a limit at 95% CL. In the fits presented here, this data is used to constrain electron flavor appearance in neutrino mode, with 10 bins used in the fit. Statistical and systematic errors for this data set are added in quadrature.

The Booster Beam Disappearance Search:

The MiniBooNE experiment also searched for ν_μ and $\bar{\nu}_\mu$ disappearance using the Booster Neutrino Beam. The neutrino (antineutrino) data set corresponded to 5.6×10^{20} (3.4×10^{20}) protons on target, producing a beam covering the neutrino energy range up to 1.9 GeV. The MiniBooNE ν_μ disappearance result provides restrictions on sterile neutrino oscillations which are comparable to those provided by the CDHS experiment, discussed below. Therefore, we include that data set in these fits. On the other hand, the $\bar{\nu}_\mu$ result was weaker due to the combination of fewer protons on target and lower cross section. The MINOS $\bar{\nu}_\mu$ CC constraint, described below, is substantially stronger, and so we do not use the MiniBooNE $\bar{\nu}_\mu$ data set.

The fit to the ν_μ data set uses 16 bins ranging up to 1900 MeV in reconstructed neutrino energy. A shape-only fit is performed, where the predicted spectrum given any set of oscillation parameters is renormalized so that the total number of predicted events, after oscillations, is equal to the total number of observed events. Then the normalized predicted spectrum is compared to the observed spectrum in the form of a χ^2 which accounts for statistical and shape-only systematic uncertainties and bin-to-bin correlations in the form of a covariance matrix.

This data set is referred to as **BNB-MB(ν dis)** in the analysis below. Fig. 2 shows that this data sets a limit at 95% CL. It should be noted that the published MiniBooNE analysis used a Pearson χ^2 method [48], and we are able to reproduce those results. However, to fold these results into our analysis, we reverted to the $\Delta\chi^2$ definition used consistently among all data sets included in the fits (see Sec. 4.2).

3.2.3 Results from Multi-GeV Conventional Short baseline ν_μ Beams

The set of multi-GeV conventional SBL ν_μ experiments is the same as was used in previous fits. Our overview of these experiments is therefore very brief.

NOMAD Appearance Search:

The NOMAD experiment [50], which ran at CERN using protons from the 450 GeV SPS accelerator, employed a conventional neutrino beamline to create a wide band 2.5 to 40 GeV neutrino energy source. These neutrinos were created with a carbon-based, low-mass, tracking detector located 600 m downstream of the target. This detector had fine spatial resolution and could search for muon-to-electron and muon-to-tau oscillations. No signal was observed in either mode. In this analysis, we use the $\nu_\mu \rightarrow \nu_e$ constraint.

This data set is referred to as **NOMAD** in the analysis below. This data set contributes 30 energy bins to the global fit. The statistical and systematic errors are added in quadrature. This experiment sets a limit at 95% CL, as seen in Fig. 1.

CCFR Disappearance Search:

The CCFR data set was taken at Fermilab in 1984 [51] with a narrow band beamline, with meson energies set to 100, 140, 165, 200, and 250 GeV, yielding ν_μ and $\bar{\nu}_\mu$ beams that ranged from 40 to 230 GeV in energy. This was a two detector disappearance search, with the near detector at 715 m and the far detector at 1116 m from the center of the 352 m long decay pipe. The calorimetric detectors were constructed of segmented iron with scintillator and spark chambers, and each had a downstream toroid to measure the muon momentum.

This data set is referred to as **CCFR84** in the analysis below. The data were published as the double ratios of the observed-to-expected rates in a near-to-far ratio. For each secondary mean setting the data are divided into three energy bins. The systematic uncertainty is assumed to be energy independent and fully correlated between the energy bins. Due to the high beam energies and short baselines, this experiment sets a limit at high Δm^2 in the muon flavor disappearance search at 95% CL, as shown in Fig. 2.

CDHS Disappearance Search:

The CDHS experiment [52] at CERN searched for ν_μ disappearance with a two-detector design of segmented calorimeters with iron and scintillator. The experiment used 19.2 GeV protons on a beryllium target to produce mesons that were subsequently focused into a 52 m decay channel. The detectors were located 130 m and 885 m downstream of the target.

This data set is referred to as **CDHS** in the analysis below. CDHS provides data and errors in 15 bins of muon energy, provided in Table 1 of Ref. [52]. We associate these bins to the neutrino energy distributions using the method described in Ref. [20]: the neutrino energy distribution for a given muon energy or range is determined via the NUANCE [53] neutrino cross section generator. The experiment has a limit at 95% CL and sets constraints that are comparable to the MiniBooNE ν_μ disappearance limit described above, but extending to slightly lower Δm^2 . See Fig. 2 for comparison.

3.2.4 Reactor and Source Experiments

The reactor experiment data set has been updated to reflect recent changes in the predicted neutrino fluxes, as discussed below. The source-based experimental data sets are both new to this paper, having been published since our last set of fits [22].

Bugey Data Set:

This analysis uses energy dependent data from the Bugey 3 reactor experiment [54]. The detector consisted of ^6Li -doped liquid scintillator, with data taken at 15, 45 and 90 m from the 2.8 GW reactor source. The detectors are taken to be point-like in the analysis.

Recently, a reanalysis of reactor $\bar{\nu}_e$ flux predictions [23, 36, 37] has led to a reinterpretation of the Bugey data. The data has transitioned from a limit on neutrino disappearance to an allowed region at 95% CL. In this analysis, we adjust the predicted Bugey flux spectra normalization according to the calculations from Ref. [23].

There are many other SBL reactor data sets in existence. However, we have chosen to use only Bugey in these fits as the measurement has the lowest combined errors. Also, any global fit to multiple reactor data sets must correctly account for the correlated systematics between them, which is beyond the scope of our fits at present.

This data set is referred to as **Bugey** in the analysis below. As shown in Fig. 3, this data set presents a signal at 95% CL. The total number of bins in the analysis are 60, with the 15 m and 45 m baselines contributing 25 bins each and the 90 m baseline contributing 10 bins, each extending from 1 to 6 MeV in positron energy. The fit follows the “normalized energy spectra” fit method detailed in Ref. [54], and χ^2 definition detailed within, which depends not only on the mass and mixing parameters we fit for, but also five large scale deformations of the positron spectrum due to systematic effects. Energy resolution and baseline smearing are taken into account. To fold in the flux normalization correction mentioned above, we update the theoretical prediction for the expected ratio by an overall normalization factor of 1.06237, 1.06197, and 1.0627 for the 15 m, 45 m, and 90 m baselines, respectively.

Gallium Calibration Data Set:

Indications of ν_e disappearance have recently been published from calibration data taken by the SAGE [33] and GALLEX [34] experiments. These were solar neutrino experiments that used Megacurie sources of ^{51}Cr and ^{37}Ar , which produce ν_e , to calibrate the detectors. Each of the two experiments had two calibration periods. The overall rates from these four measurements are consistent, and show an overall deficit that has been reported to be consistent with electron flavor disappearance [27, 55]. We use the four ratios of calibration data to expectation, as reported in Ref. [27], Table 2: 1.00 ± 0.10 , 0.81 ± 0.10 , 0.95 ± 0.12 and 0.79 ± 0.10 . These correspond to the two periods from GALLEX and the two periods from SAGE, respectively. Our analysis of this data set, referred to as **Gallium** below, follows that of Ref. [27]; a 4-bin fit to the above measured calibration period rates is used. The predicted rates, after oscillations, are obtained by averaging the oscillation probabilities taking into account the detector geometry, the location of the source within the detector, and the neutrino energy distribution for each source (energy line and branching fraction). The neutrino energies are approximately 430 and 750 keV for ^{51}Cr , and 812 keV for ^{37}Ar . The data result in a limit at 95% CL, as shown in Fig. 3.

3.2.5 Long Baseline Experimental Results Contributing to the Fits

While this study concentrates mainly on results from SBL experiments, the data from experiments with baselines of hundreds of kilometers can be valuable. At such long baselines, the ability to identify the Δm^2 associated with any observed oscillation has disappeared due to the rapid oscillations. However,

these experiments can place strong constraints on the mixing parameters. New to this paper is the inclusion of the MINOS $\bar{\nu}_\mu$ CC constraint. We have included the atmospheric data set in our previous fits [20–22].

We note two long baseline results not included in this analysis. First, we have dropped the Chooz data set that was included in previous fits [20–22] due to the discovery that $\sin^2 2\theta_{13}$ is large [12–16], which significantly complicates the use of this data for SBL oscillation searches. Second, the recent muon-flavor disappearance results from IceCube [56] were published too late to be included in this iteration of fits. However, the MiniBooNE and MINOS muon-flavor disappearance results are more stringent than the IceCube limits, and so we do not expect this to affect the results.

MINOS $\bar{\nu}_\mu$ CC Disappearance Search:

MINOS is a muon flavor disappearance experiment featuring two (near and far) iron-scintillator segmented calorimeter style detectors in the NuMI beamline (described above) at Fermilab. The near detector is located 1 km from the target while the far detector is located 730 m away. The wide band beam is peaked at about 4 GeV.

MINOS ran in both neutrino and antineutrino mode. We employ the antineutrino data in our fits as it constrains the allowed region for muon antineutrino disappearance when we divide the data sets into neutrino vs. antineutrino fits. The MINOS neutrino mode disappearance limit is not as restrictive as the atmospheric result and so only the antineutrino data set is utilized.

This result is referred to as **MINOS-CC** in the analysis below. The data present a limit at 95% CL as discussed above and shown in Fig. 2. In our analysis of MINOS-CC, we fit both the antineutrino (right sign) data published by MINOS in antineutrino mode running [57] and the antineutrino (wrong sign) data published by MINOS in neutrino mode running [58]. The right sign data are considered in 12 bins from 0 to 20 GeV, and the wrong sign in 13 bins from 0 to 50 GeV. We account for possible oscillations in the near detector due to high Δm^2 values by using the ratio of the oscillation probabilities at the far and near detectors for each mass and mixing model. As MINOS is sensitive to Δm_{atm}^2 , we add an extra mass state to the oscillation probability using the best-fit atmospheric mass and mixing parameters from the MINOS experiment [10]. The data points and systematic errors are taken from [57] and [58].

Atmospheric Constraints on ν_μ Disappearance Used in Fits:

Atmospheric neutrinos are produced when cosmic rays interact with nuclei in the atmosphere to produce showers of mesons. The neutrino pathlength varies from a few to 12,800 km, while neutrino energies range from sub- to few-GeV. Thus, this is a long baseline source with sensitivity to primarily ν_μ disappearance and effectively no sensitivity to Δm_{ij}^2 . The former is a consequence of the atmospheric neutrino flux composition and the detector technology used in atmospheric experiments. Thus, atmospheric neutrino measurements and long baseline accelerator-based ν_μ disappearance experiments constrain the same parameters, and are treated in our fits in a similar way.

As with our past fits, we include atmospheric constraints following the prescription of Ref. [59]. We refer to this data set in our fits as **ATM**. This makes use of two data sets: (1) 1489 days of Super-K muon-like and electron-like events with energies in the sub- to multi-GeV range, taking into account atmospheric flux predictions from [60] and treating systematic uncertainties according to [61];

and (2) ν_μ disappearance data from the long baseline, accelerator-based experiment K2K [62–64]. The atmospheric constraint is implemented in the form of a χ^2 available to us as a function of the parameter d_μ , which depends on the muon flavor composition of m_4 , m_5 , and m_6 as follows:

$$d_\mu = \frac{1 - \sqrt{1 - 4A}}{2}, \quad (15)$$

where

$$A = (1 - |U_{\mu 4}|^2 - |U_{\mu 5}|^2 - |U_{\mu 6}|^2)(|U_{\mu 4}|^2 + |U_{\mu 5}|^2 + |U_{\mu 6}|^2) + |U_{\mu 4}|^2 |U_{\mu 5}|^2 + |U_{\mu 4}|^2 |U_{\mu 6}|^2 + |U_{\mu 5}|^2 |U_{\mu 6}|^2. \quad (16)$$

The atmospheric constraints set a limit at 95% CL as shown in Fig. 2.

4 Analysis Description

The analysis method follows the formalism described in Sec. 2.3, and fits are performed to each of the (3+1), (3+2), and (3+3) hypotheses separately.

4.1 Fit Parameters

The independent parameters considered in the (3+1) fit are Δm_{41}^2 , representing the splitting between the (degenerate) first three mass eigenstates and the fourth mass eigenstate, and $|U_{e4}|$ and $|U_{\mu 4}|$, representing the electron and muon flavor content in the fourth mass eigenstate, which are assumed to be small. The (3+2) model introduces an additional, fifth mass eigenstate, where $\Delta m_{51}^2 \geq \Delta m_{41}^2$, two additional mixing parameters, $|U_{e5}|$ and $|U_{\mu 5}|$, as well as the CP-violating phase ϕ_{54} , defined by Eq. 7. The (3+3) model includes all the previous parameters and yet another, sixth mass eigenstate, described by Δm_{61}^2 , where $\Delta m_{61}^2 \geq \Delta m_{41}^2$, Δm_{51}^2 , two additional mixing parameters, $|U_{e6}|$ and $|U_{\mu 6}|$, as well as two more CP-violating phases, ϕ_{46} and ϕ_{56} . The above model parameters are allowed to freely vary within the following ranges: Δm_{41}^2 , Δm_{51}^2 and Δm_{61}^2 within 0.01-100 eV², $|U_{\alpha i}|$ within 0-0.5, and ϕ_{ij} within 0-2 π , with the exception that for the $|U_{\alpha i}|$ there are additional constraints imposed on the mixing parameters in order to conserve unitarity of the full $(3+N) \times (3+N)$ mixing matrix in each scenario, as described in Sec. 2.3.

4.2 Fitting Method

The fitting method closely follows what has been done in Ref. [21]. Given an oscillation model, (3+1), (3+2), or (3+3), the corresponding independent oscillation parameters are randomly generated within their allowed range, and then varied via a Markov Chain χ^2 minimization procedure [65]. Each independent parameter x is generated and varied according to

$$x = x_{old} + s(R - 0.5)(x_{min} - x_{max}), \quad (17)$$

where x_{old} is the value of parameter x previously tested in the χ^2 minimization chain, x_{min} and x_{max} represent the boundaries on the parameter x as described in Sec. 4.1, R is a random number between 0 and 1, which is varied as one steps from x_{old} to x , and s is the “stepsize”, a parameter of the Markov Chain. By definition within the Markov Chain minimization method, the point is accepted based only

on the point directly preceding it. The acceptance of any new point \vec{x} in the chain, where \vec{x} is the new point in the oscillation parameter space, is determined by:

$$P = \min(1, e^{-(\chi^2 - \chi_{old}^2)/T}) , \quad (18)$$

where T is the Markov Chain parameter “temperature”. The step size and temperature control how quickly the Markov Chain diffuses toward the minimum χ^2 value. At every step in the chain, which corresponds to a point in the oscillation parameter space, \vec{x} , a χ_x^2 is calculated by summing together the individual $\chi_{x,d}^2$ contributed from each data set d included in the fit, where d denotes any of the data sets described in Sec. 3.2.

In any given fit, we define possible signal indications at 90% and 99% CL by marginalizing over the full parameter space, and looking for closed contours formed about a global minimum, χ_{min}^2 , when projected onto any two-dimensional parameter space, assuming only two (2) degrees of freedom. We use the standard, two degree of freedom $\Delta\chi^2$ cuts of 4.61 for exploring allowed 90% CL regions, 5.99 for exploring allowed 95% CL regions (used only for Figs. 1, 2 and 3), and 9.21 for 99% CL regions. If the null point ($U_{\alpha i}, U_{\beta i} = 0$) is allowed at $> 95\%$ CL, we instead proceed with drawing one-dimensional raster scan limits, obtained with the standard $\Delta\chi^2$ cuts of 2.70, 3.84 and 6.63 for 90%, 95% (used only for Figs. 1, 2 and 3), and 99% CL, respectively.

4.3 Parameter Goodness-of-Fit Test

In any given fit, in addition to a standard χ^2 -probability, which is quoted for the global χ_{min}^2 and number of degrees of freedom in the fit, we also report statistical compatibility comparisons using the Parameter Goodness-of-fit test (PG test) from Ref. [66]. This test reduces the bias imposed toward data sets with a large number of bins in the standard χ^2 - probability, in order to calculate the compatibility between data sets simply on the basis of preferred parameters. The compatibility, or PG (%), can be calculated to quantify compatibility between any two or more data sets, or between combinations of data sets, according to

$$\chi_{PG}^2 = \chi_{min,combined}^2 - \sum_i \chi_{min,d}^2 , \quad (19)$$

where the $\chi_{min,combined}^2$ is the χ^2 -minimum of the combined fit of the data sets in consideration, and $\chi_{min,d}^2$ is the χ^2 of each data set or combination of data sets included in the combined fit when fit individually. The number of degrees of freedom (ndf_{PG}) for the PG test is given by

$$ndf_{PG} = \sum_d N_{pd} - N_{p_{combined}} . \quad (20)$$

Here, N_{pd} represents the number of *independent* parameters involved in the fit of a particular data set and $N_{p_{combined}}$ represents the number of *independent* parameters involved in the global fit.

5 Results

This section presents the results of the analysis for the (3+1), (3+2), and (3+3) sterile neutrino models. For reference, information about the data sets used in the analyses is provided in Table 1. Tables 2 and 3 summarize the results of the fits, which will be described in more detail below. Table 2 gives

Tag	Section	Process	ν vs. $\bar{\nu}$	App vs. Dis
LSND	3.2.1	$\bar{\nu}_\mu \rightarrow \bar{\nu}_e$	$\bar{\nu}$	App
KARMEN	3.2.1	$\bar{\nu}_\mu \rightarrow \bar{\nu}_e$	$\bar{\nu}$	App
KARMEN/LSND(xsec)	3.2.1	$\nu_e \rightarrow \nu_e$	ν	Dis
BNB-MB(ν app)	3.2.2	$\nu_\mu \rightarrow \nu_e$	ν	App
BNB-MB($\bar{\nu}$ app)	3.2.2	$\bar{\nu}_\mu \rightarrow \bar{\nu}_e$	$\bar{\nu}$	App
NuMI-MB(ν app)	3.2.2	$\nu_\mu \rightarrow \nu_e$	ν	App
BNB-MB(ν dis)	3.2.2	$\nu_\mu \rightarrow \nu_\mu$	ν	Dis
NOMAD	3.2.3	$\nu_\mu \rightarrow \nu_e$	ν	App
CCFR84	3.2.3	$\nu_\mu \rightarrow \nu_\mu$	ν	Dis
CDHS	3.2.3	$\nu_\mu \rightarrow \nu_\mu$	ν	Dis
Bugey	3.2.4	$\bar{\nu}_e \rightarrow \bar{\nu}_e$	$\bar{\nu}$	Dis
Gallium	3.2.4	$\nu_e \rightarrow \nu_e$	ν	Dis
MINOS-CC	3.2.5	$\bar{\nu}_\mu \rightarrow \bar{\nu}_\mu$	$\bar{\nu}$	Dis
ATM	3.2.5	$\nu_\mu \rightarrow \nu_\mu$	ν	Dis

Table 1: Data sets used in the fits and their corresponding use in the analysis. Column 1 provides the tag for the data. Column 2 references the description in Sec. 3.2. Column 3 lists the relevant oscillation process. Column 4 lists which data sets are included in the neutrino vs. antineutrino analyses and column 5 lists which data sets are included in the appearance vs. disappearance study.

the fit results for the overall global fits and for various combinations of data sets. When interpreting compatibilities, one should keep in mind that, along with a high compatibility among the individual data sets in a global fit, high compatibility values among groups of data sets is also important. Finally, Table 3 provides the parameters for the best-fit points for each of the models.

5.1 (3+1) Fit Results

For a (3+1) model, three parameters are determined: Δm_{41}^2 , $|U_{e4}|$, and $|U_{\mu 4}|$. A global (3+1) fit of all of the experiments (Fig. 4) yields a χ^2 - probability of 55% but a very low compatibility of 0.043%, indicating a low compatibility among all individual data sets. Contrasting the good result from the χ^2 test to the poor compatibility illustrates how the χ^2 test can be misleading. As discussed above, this is due to some data sets dominating others due to the number of bins in the fit, many of which may not have strong oscillation sensitivity. It is for this reason that most groups fitting for sterile neutrinos now use the PG test as the figure of merit.

In order to understand the source of the poor compatibility, the data sets are subdivided, as shown in Table 2, into separate neutrino and antineutrino results. Within each of these categories, the compatibility values are 2.2% and 11% for neutrinos and antineutrinos respectively, which are reasonably good. However, the two data sets favor very different oscillation parameters, as is seen in Table 3 and Fig. 5. This leads to a very low compatibility of 0.14% when the neutrino and antineutrino data are compared. The separation of the data sets into appearance and disappearance also shows a strong incompatibility leading to an even lower compatibility of 0.013%. These results imply that the (3+1) model is not sufficient to describe all data sets simultaneously.

Looking at the best-fit values of Table 3, one also sees that two different Δm_{41}^2 values are preferred

for neutrino vs. antineutrino and for appearance vs. disappearance. This leads one to suspect that the data would prefer at least two mass splittings between the mostly active and the mostly sterile states and, thus, encourages the consideration of a (3+2) interpretation [20]. Moreover, a (3+2) model allows the introduction of a CP-violating phase, which can address the differences between neutrino and antineutrino data sets [21]. Therefore, these results lead us to abandon (3+1), and move on to testing the (3+2) hypothesis. It should be noted that the shortcomings of the (3+1) model have now been established by a number of independent analyses [20, 22, 23, 67–69].

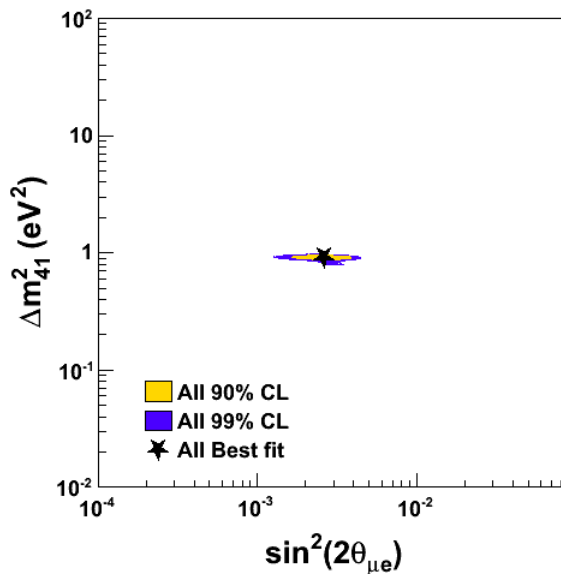


Figure 4: The Δm_{41}^2 vs. $\sin^2 2\theta_{\mu e}$ allowed space from fits to all data—neutrino and antineutrino—in a (3+1) model.

5.2 (3+2) Fit Results

In a (3+2) model, there are seven parameters to determine: Δm_{41}^2 , Δm_{51}^2 , $|U_{e4}|$, $|U_{\mu 4}|$, $|U_{e5}|$, $|U_{\mu 5}|$, and ϕ_{54} . The best-fit values for these parameters from global fit to all data sets are given in Table 3. The 90% and 99% CL contours in marginalized $(\Delta m_{41}^2, \Delta m_{51}^2)$ space can be seen in Fig. 7.

Adding a second mass eigenstate reduces the tension seen in the (3+1) fits, bringing the overall compatibility to 13% (see Table 2), and reducing the χ^2 of the global fit by 12.4 units, for four extra parameters introduced to the fit. For this compatibility test, the BNB-MB(ν app) data set has the worst χ^2 -probability. When considered by itself, the BNB-MB(ν app) data set gives a constrained (see Sec 3.2.2) χ^2 (dof) of 19.2 (4) for the global best-fit parameters, which corresponds to a χ^2 -probability of 0.07%. This is one of the first indications that the MiniBooNE neutrino data has some tension with the other data sets.

The need to introduce a CP-violating phase was established in previous studies of global fits [22]. This term affects only fits involving appearance data sets and results in a difference in the oscillation

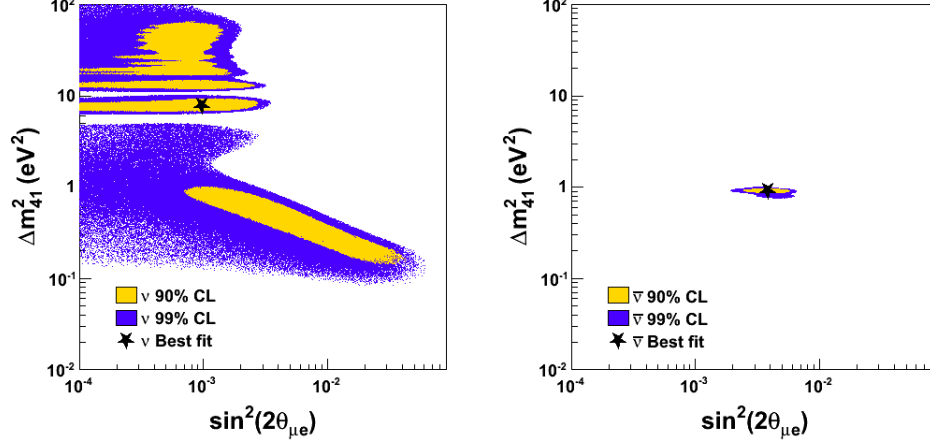


Figure 5: The Δm_{41}^2 vs. $\sin^2 2\theta_{\mu e}$ allowed space from fits to neutrino (left) and antineutrino (right) data in a (3+1) model.

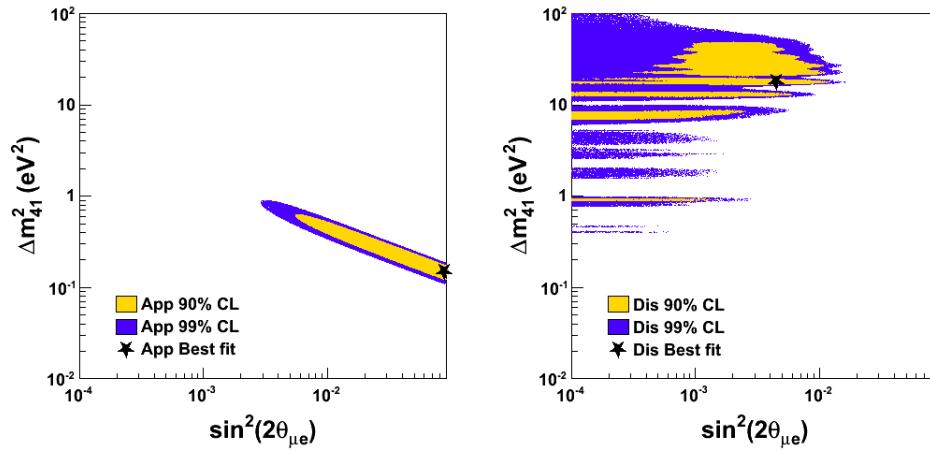


Figure 6: The Δm_{41}^2 vs. $\sin^2 2\theta_{\mu e}$ allowed space from fits to appearance (left) and disappearance (right) data in a (3+1) model.

	χ^2_{min} (dof)	χ^2_{null} (dof)	P_{best}	P_{null}	χ^2_{PG} (dof)	PG (%)
3+1						
All	233.9 (237)	286.5 (240)	55%	2.1%	54.0 (24)	0.043%
App	87.8 (87)	147.3 (90)	46%	0.013%	14.1 (9)	12%
Dis	128.2 (147)	139.3 (150)	87%	72%	22.1 (19)	28%
ν	123.5 (120)	133.4 (123)	39%	25%	26.6 (14)	2.2%
$\bar{\nu}$	94.8 (114)	153.1 (117)	90%	1.4%	11.8 (7)	11%
App vs. Dis	-	-	-	-	17.8 (2)	0.013%
ν vs. $\bar{\nu}$	-	-	-	-	15.6 (3)	0.14%
3+2						
All	221.5 (233)	286.5 (240)	69%	2.1%	63.8 (52)	13%
App	75.0 (85)	147.3 (90)	77%	0.013%	16.3 (25)	90%
Dis	122.6 (144)	139.3 (150)	90%	72%	23.6 (23)	43%
ν	116.8 (116)	133.4 (123)	77%	25%	35.0 (29)	21%
$\bar{\nu}$	90.8 (110)	153.1 (117)	90%	1.4%	15.0 (16)	53%
App vs. Dis	-	-	-	-	23.9 (4)	0.0082%
ν vs. $\bar{\nu}$	-	-	-	-	13.9 (7)	5.3%
3+3						
All	218.2 (228)	286.5 (240)	67%	2.1%	68.9 (85)	90%
App	70.8 (81)	147.3 (90)	78%	0.013%	17.6 (45)	100%
Dis	120.3 (141)	139.3 (150)	90%	72%	24.1 (34)	90%
ν	116.7 (111)	133.4 (123)	34%	25%	39.5 (46)	74%
$\bar{\nu}$	90.6 (105)	153 (117)	84%	1.4%	18.5 (27)	89%
App vs. Dis	-	-	-	-	28.3 (6)	0.0081%
ν vs. $\bar{\nu}$	-	-	-	-	110.9 (12)	53%

Table 2: The χ^2 values, degrees of freedom (dof) and probabilities associated with the best-fit and null hypothesis in each scenario. Also shown are the results from the Parameter Goodness-of-fit tests. P_{best} refers to the χ^2 -probability at the best fit point and P_{null} refers to the χ^2 -probability at null.

3+1	Δm_{41}^2	$ U_{\mu 4} $	$ U_{e 4} $
All	0.92	0.17	0.15
App	0.15	0.39	0.39
Dis	18	0.18	0.18
ν	7.8	0.059	0.26
$\bar{\nu}$	0.92	0.23	0.13

3+2	Δm_{41}^2	Δm_{51}^2	$ U_{\mu 4} $	$ U_{e 4} $	$ U_{\mu 5} $	$ U_{e 5} $	ϕ_{54}
All	0.92	17	0.13	0.15	0.16	0.069	1.8π
App	0.31	1.0	0.31	0.31	0.17	0.17	1.1π
Dis	0.92	18	0.015	0.12	0.17	0.12	N/A
ν	7.6	17.6	0.05	0.27	0.18	0.052	1.8π
$\bar{\nu}$	0.92	3.8	0.25	0.13	0.12	0.079	0.35π

3+3	Δm_{41}^2	Δm_{51}^2	Δm_{61}^2	$ U_{\mu 4} $	$ U_{e 4} $	$ U_{\mu 5} $	$ U_{e 5} $	$ U_{\mu 6} $	$ U_{e 6} $	ϕ_{54}	ϕ_{64}	ϕ_{65}
All	0.90	17	22	0.12	0.11	0.17	0.11	0.14	0.11	1.6π	0.28π	1.4π
App	0.15	1.8	2.7	0.37	0.37	0.12	0.12	0.12	0.12	1.4π	0.32π	0.94π
Dis	0.92	7.2	18	0.013	0.12	0.019	0.16	0.15	0.069	N/A	N/A	N/A
ν	13	17	26	0.076	0.24	0.16	0.067	0.10	0.017	1.1π	1.8π	0.037π
$\bar{\nu}$	7.5	9.1	18	0.024	0.28	0.098	0.11	0.18	0.029	1.8π	2.0π	0.61π

Table 3: The oscillation parameter best-fit points in each scenario considered. The values of Δm^2 shown are in units of eV^2

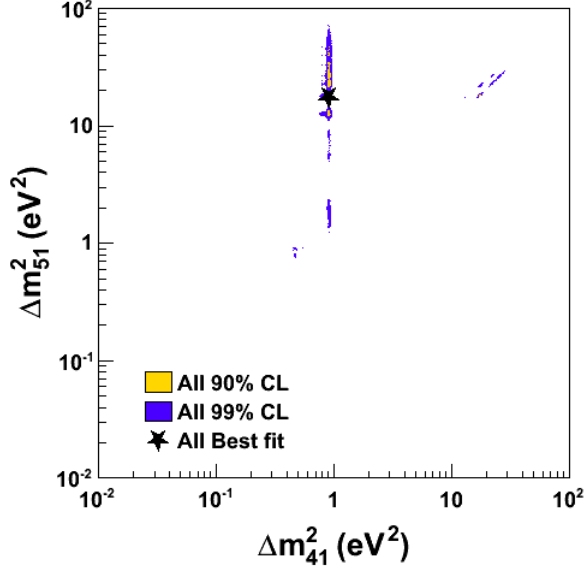


Figure 7: The Δm_{51}^2 vs. Δm_{41}^2 correlations from fits to all data in a (3+2) model.

probabilities for $\nu_\mu \rightarrow \nu_e$ vs. $\bar{\nu}_\mu \rightarrow \bar{\nu}_e$. In particular, previous studies considered CP-violating fits in an attempt to reconcile the MiniBooNE neutrino appearance results with the MiniBooNE and LSND antineutrino appearance results.

Table 2 also gives the results for combinations of the data sets for cross comparison. We find that the separate neutrino and antineutrino data set fits remain in good agreement and that the compatibility between the neutrino and antineutrino data sets has risen to 5.3%—a significant improvement over the (3+1) result. The best-fit values and allowed regions are shown in Table 3 and in Fig. 8 respectively.

While the neutrino vs. antineutrino discrepancy has been somewhat reduced, Table 2 points out a second important problem. The appearance and disappearance data sets still have very poor compatibility (0.0082%), even in a (3+2) model. The poor compatibility can be partially traced to a discrepancy in the preferred mass splittings for these two data sets. As reported in Table 3, the appearance data sets prefer a low (0.31 eV²) and a medium (1.0 eV²) mass-squared splitting while the disappearance data sets prefer a medium (0.92 eV²) and a high (18 eV²) splitting. This is also illustrated in Fig. 9. This suggests that three mass splittings may be required to reconcile appearance and disappearance results, and motivates the consideration of a (3+3) model.

5.3 (3+3) Fit Results

For a (3+3) model, there are 12 model parameters to be determined: $\Delta m_{41}^2, \Delta m_{51}^2, \Delta m_{61}^2, |U_{e4}|, |U_{\mu 4}|, |U_{e5}|, |U_{\mu 5}|, |U_{e6}|, |U_{\mu 6}|, \phi_{54}, \phi_{64}$, and ϕ_{65} . Adding a third mass eigenstate does not significantly change the global fit χ^2_{min} ; however, the tension between the individual data set fits is further reduced, raising the compatibility from 13%, in (3+2), to 90%. The neutrino and antineutrino compatibility rises by an order of magnitude from the (3+2) value to 53%, indicating that the (3+3) model can better

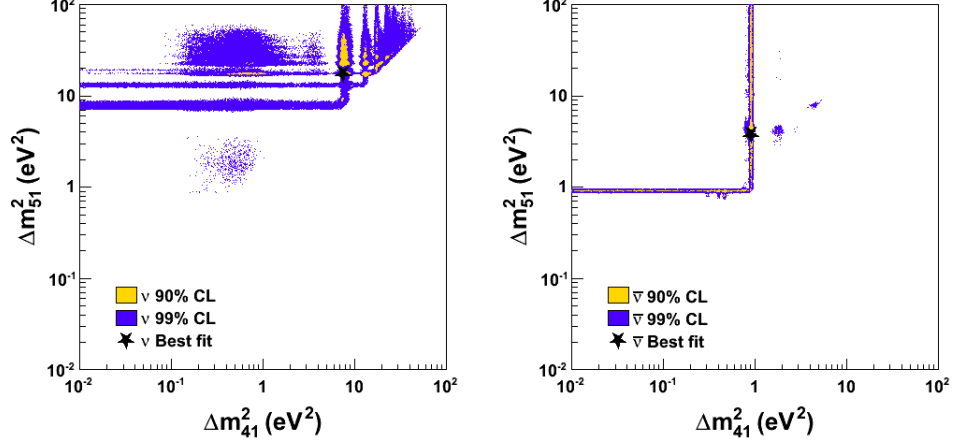


Figure 8: The Δm_{51}^2 vs. Δm_{41}^2 correlations from fits to neutrino (left) and antineutrino (right) data in a (3+2) model.

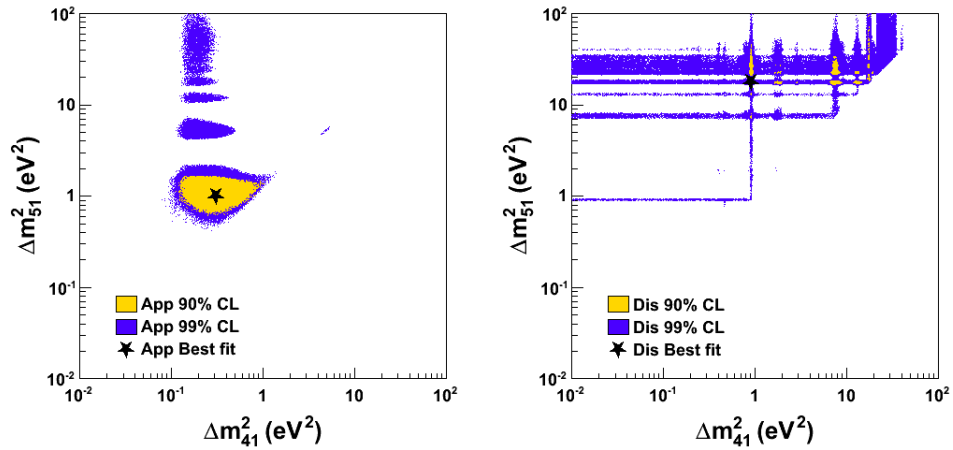


Figure 9: The Δm_{51}^2 vs. Δm_{41}^2 correlations from fits to appearance (left) and disappearance (right) data in a (3+2) model.

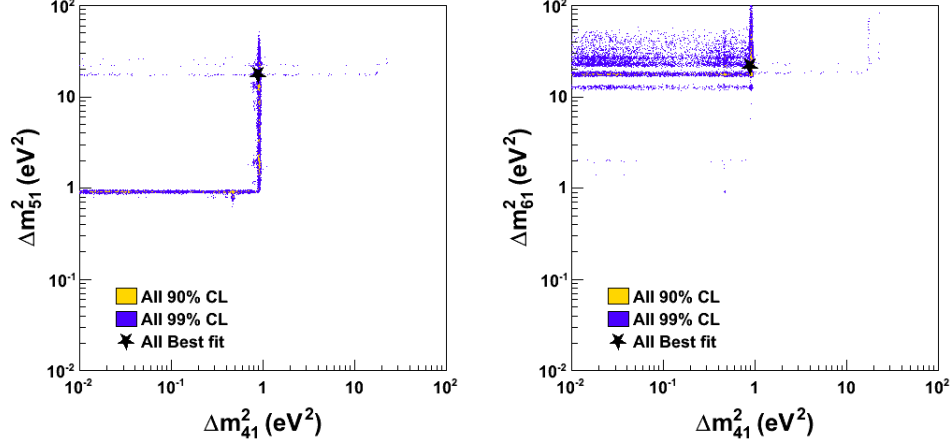


Figure 10: The Δm_{51}^2 vs. Δm_{41}^2 and Δm_{61}^2 vs. Δm_{41}^2 correlations from fits to all data in a (3+3) model.

accommodate the differences in these data sets.

It is interesting to note that the (3+3) fit prefers an “inverted hierarchy” among the three mostly sterile states, with $\Delta m_{54}^2 = m_5^2 - m_4^2 = 16 \text{ eV}^2$ and $\Delta m_{65}^2 = m_6^2 - m_5^2 = 5.0 \text{ eV}^2$. The overall splitting relative to the three mostly-active states is $\Delta m_{41}^2 = m_4^2 - m_1^2 = 0.90 \text{ eV}^2$.

The one puzzling discrepancy for the (3+3) fits is the tension still exhibited by the appearance vs. disappearance data sets, where the compatibility remains low, at less than 0.01%. We find that an important source of this incompatibility is the BNB-MB(ν app) and BNB-MB($\bar{\nu}$ app) data sets. The BNB-MB(ν app) data set has fairly small statistical and systematic uncertainties and therefore has a large impact on the fits and compatibility calculations. This is shown in Fig. 13 where the MB data agrees well with the appearance-only fit but disagrees with the overall global fit. Removing both the BNB-MB(ν app) and BNB-MB($\bar{\nu}$ app) sets raises the compatibility to 3.5%, corresponding to over two orders of magnitude improvement. It has been known since the first MiniBooNE publication [18] that the the BNB-MB(ν app) data was fairly consistent with no oscillations above 475 MeV; however, a significant low-energy excess was present below this energy. The energy dependence of the BNB-MB(ν app) excess does not fit very well with oscillation models extracted from fits to global data sets, unless very low Δm_{ij}^2 with large mixing elements $|U_{ei}|$ and $|U_{\mu i}|$ are involved in the fit. This may lead to the poor compatibility when included in appearance vs. disappearance comparisons. Other possible explanations for this incompatibility include downward fluctuations of the BNB-MB(ν app) data in the higher energy region or some other process contributing part of the low energy excess such as those suggested in Refs. [70, 71].

Statistical issues could be addressed with more MiniBooNE neutrino data that may become available over the next several years. In addition, the MicroBooNE experiment, which is expected to start running in 2014, will provide more information on the low-energy excess events and answer the question of whether the excess is associated with outgoing electrons or photons [72].

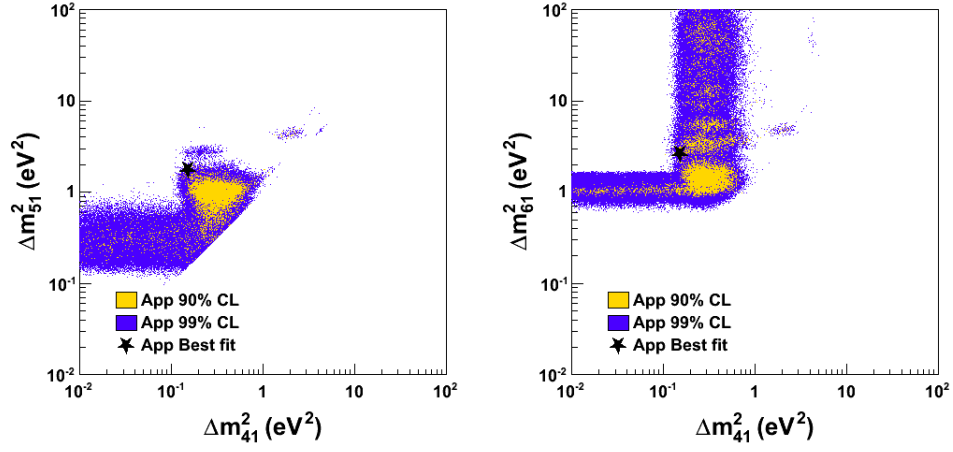


Figure 11: The Δm_{51}^2 vs. Δm_{41}^2 and Δm_{61}^2 vs. Δm_{41}^2 correlations from fits to appearance data in a (3+3) model.

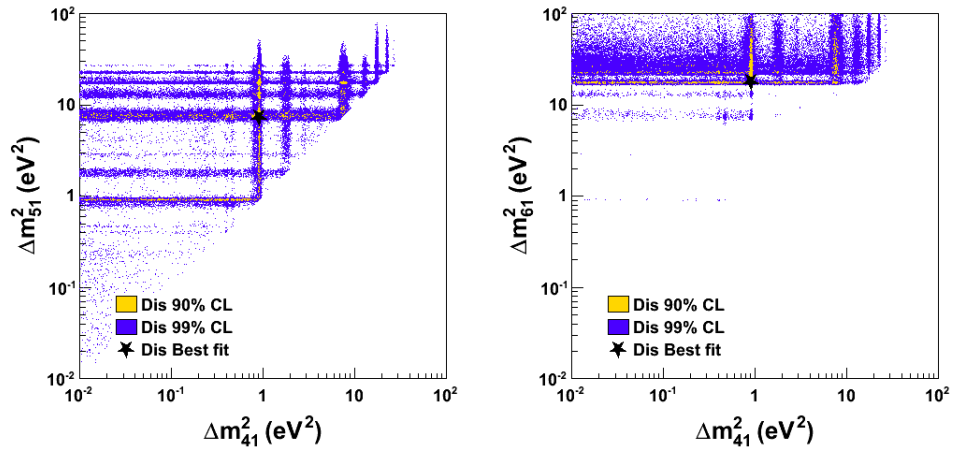


Figure 12: The Δm_{51}^2 vs. Δm_{41}^2 and Δm_{61}^2 vs. Δm_{41}^2 correlations from fits to disappearance data in a (3+3) model.

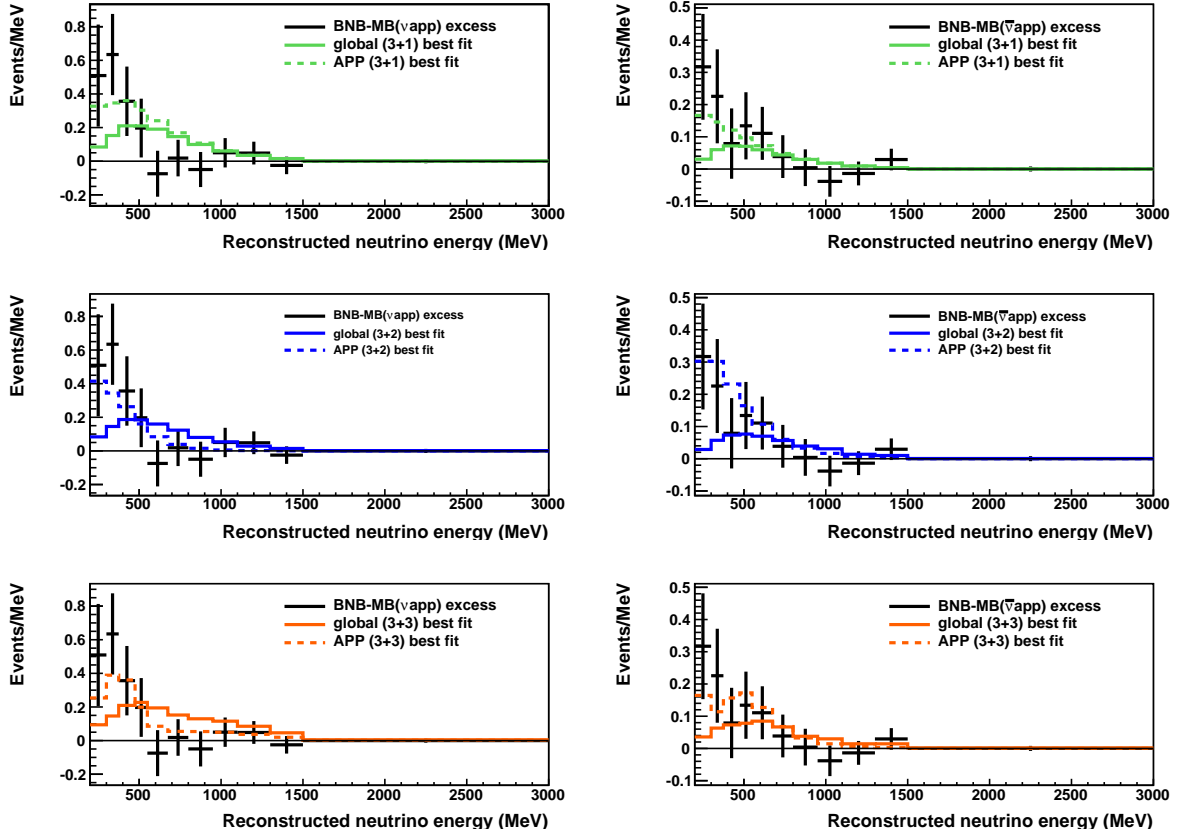


Figure 13: A comparison of the BNB-MB(ν_{app}) and BNB-MB($\bar{\nu}_{app}$) excess data with the global best-fit oscillation signal predictions (solid colored lines) and with the appearance only best-fit predictions (dashed colored lines) for each of the models, (3+1), (3+2), and (3+3). The error bars on the excess correspond to data statistical and unconstrained background systematic errors, added in quadrature.

5.4 Summary of Results

The sterile neutrino fits to global data sets show that a (3+1) model is inadequate; multiple Δm_{ij}^2 values are needed along with CP-violating effects to explain the neutrino vs. antineutrino differences. A (3+2) model improves significantly on the (3+1) results but still shows some tension for the neutrino vs. antineutrino compatibility and cannot explain the appearance vs. disappearance differences. Among the three models considered, the (3+3) model gives the highest compatibility among the various data set combinations but still has poor appearance vs. disappearance compatibility. The BNB-MB(ν app) (and BNB-MB($\bar{\nu}$ app)) data set is a prime contributor to this incompatibility and additional experimental information in this region should be available soon. Figure 13 gives a comparison of the BNB-MB(ν app) and BNB-MB($\bar{\nu}$ app) data with the global best-fit predictions and with the appearance-only best-fit predictions for each of the three models, (3+1), (3+2), and (3+3). One clearly sees that the appearance-only fit describes the data very well, especially for the (3+3) model. On the other hand, the global fit prediction is significantly below the data at low energy, which contributes to the poor appearance vs. disappearance compatibility.

In summary, out of the three sterile neutrino oscillation hypotheses considered in the analysis, we find that a (3+3) model provides the best description, although the MiniBooNE appearance data continue to raise issues within the fits. As has been shown before, (3+1) scenarios provide a poor fit to the data, and should not be emphasized. We therefore recommend continued investigations of (3+2) and (3+3) scenarios.

6 The Future

Establishing the existence of sterile neutrinos would have a major impact on particle physics. Motivated by this opportunity, there are a number of existing and planned experiments set to probe the parameter space indicative of one or more sterile neutrinos. Such experiments are necessary in order to confirm or refute the observed anomalies in the $\Delta m^2 \sim 1 \text{ eV}^2$ region. The new experiments are being designed to have improved sensitivity, with the goal of 5σ sensitivity and the ability to observe oscillatory behavior in L and/or E within a single or between multiple detectors. In these experiments, the oscillation signal needs to be clearly separated from any backgrounds.

Sterile neutrino oscillation models are based on oscillations associated with mixing between active and sterile states and demand that there be both appearance and disappearance. It is therefore imperative that the future program explore both of these oscillation types. Establishing sterile neutrinos will require that the disappearance and appearance rates are compatible with sterile neutrino oscillation models. Future experiments will search for evidence of sterile neutrino(s) using a variety of neutrino creation sources: (1) pion/muon DIF (e.g., Refs. [72–77]), (2) pion or kaon DAR (e.g., Refs. [78–82]), (3) unstable isotopes (e.g., Refs. [15, 83–86]), (4) atmospheric (see Ref. [23]), and (5) nuclear reactors (e.g., Refs. [87, 88]). All of these experiments are under development and the sensitivities are likely to change. Therefore, rather than displaying sensitivity curves for each future program, we instead focus on the conceptual ideas behind the experiments. Unless otherwise mentioned, the experiments below will provide “significant” sensitivity to a large portion of the favored sterile neutrino parameter space through searches for neutrino disappearance and/or appearance.

6.1 The Importance of the L/E Signature from Multiple Experiments

Ultimately, in order to determine if there are zero, one, two, or three sterile states contributing to oscillations in SBL experiments, it will be necessary to demonstrate the expected L/E -dependent oscillation probabilities discussed in Sec. 2.3. Assuming that the SBL anomalies are confirmed, a consistent L/E dependence is the only signature which is distinct for oscillations, and excludes other exotic explanations such as CPT violation [22], decays [89], and Lorentz violation [90]. The ideal experiment would reconstruct the oscillation wave as a function of L/E [91]. The combined information from many experiments, however, is more suitable for covering the widest possible range in L/E as well as providing valuable flavor and neutrino vs. antineutrino information.

The three models, (3+1), (3+2) and (3+3) have distinct signatures as a function of L/E . To illustrate this, we consider the case of a hypothetical experiment with 10% resolution in L/E , assuming the best-fit values presented in Table 3. In the case of (3+1), as shown in Fig. 14, the disappearance (appearance) probabilities shown on the left (right), have maxima and minima that evolve monotonically to $P = 1/2 \sin^2(2\theta)$, the long baseline limit discussed in Sec. 2.2. This can be contrasted with Figs. 15 and 16, where the structure of the oscillation wave, in the approach to the long baseline limit, is more “chaotic” due to the interference between the various mass splitting terms.

In Figs. 14, 15, and 16, the two curves on the disappearance plots on the left refer to muon and electron flavor, respectively. As the theory is CPT-conserving, these disappearance curves should be identical for neutrinos and antineutrinos. The appearance curves on the right also show the importance of neutrino and antineutrino running, which can lead to very different L/E dependencies for the three models, and constrain CP-violating parameters.

In summary, it seems very unlikely that any *single* future experiment will be able to differentiate

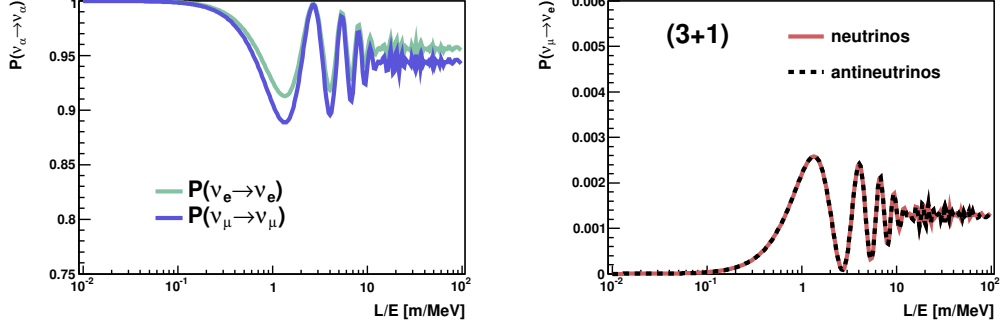


Figure 14: The (3+1) oscillation probabilities for the global best fit (“all” data sets) values in Table 3 with 10% resolution in L/E .

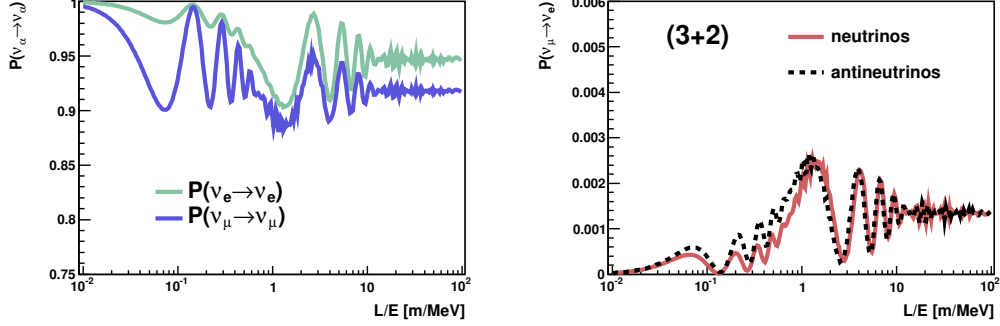


Figure 15: The (3+2) oscillation probabilities for the global best fit (“all” data sets) values in Table 3 with 10% resolution in L/E .

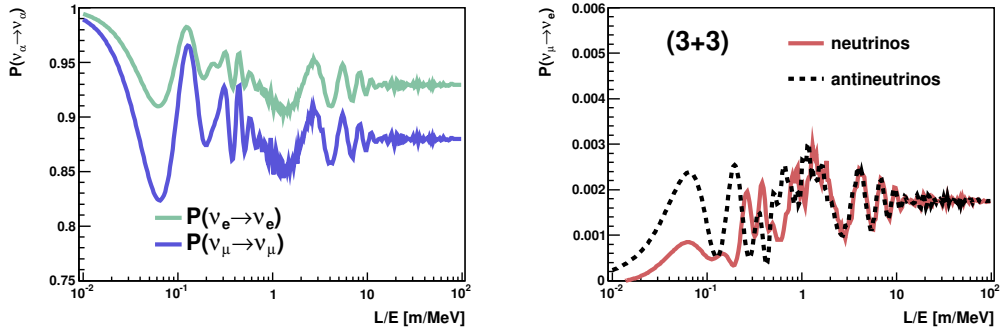


Figure 16: The (3+3) oscillation probabilities for the global best fit (“all” data sets) values in Table 3 with 10% resolution in L/E .

between the sterile neutrino models. Multiple experiments looking at different oscillation channels and covering a wide range of L/E regions are required. Thus, the consideration of many independent and relatively modest-size experiments, such as those listed in Table 4, is essential.

Source	App/Dis	Channel	Experiment
Reactor	Dis	$\bar{\nu}_e \rightarrow \bar{\nu}_e$	Nucifer, Stereo, SCRAMM, NIST, Neutrino4, DANSS
Radioactive	Dis	$\nu_e \rightarrow \nu_e \quad \bar{\nu}_e \rightarrow \bar{\nu}_e$	Baksan, LENS, Borexino, SNO+, Ricochet, CeLAND, Daya Bay
Accelerator-based isotope	Dis	$\bar{\nu}_e \rightarrow \bar{\nu}_e$	IsoDAR
Pion / Kaon DAR	App & Dis	$\bar{\nu}_\mu \rightarrow \bar{\nu}_e \quad \nu_e \rightarrow \nu_e$ $\nu_\mu \rightarrow \nu_e$	OscSNS, DAE δ ALUS, KDAR
Accelerator (Pion DIF)	App & Dis	$\nu_\mu \rightarrow \nu_e \quad \bar{\nu}_\mu \rightarrow \bar{\nu}_e$ $\nu_\mu \rightarrow \nu_\mu \quad \bar{\nu}_\mu \rightarrow \bar{\nu}_\mu$	MINOS+, MicroBooNE, LAr1kton+MicroBooNE, CERN SPS
Low-energy ν -Factory	App & Dis	$\nu_e \rightarrow \nu_\mu \quad \bar{\nu}_e \rightarrow \bar{\nu}_\mu$ $\nu_\mu \rightarrow \nu_\mu \quad \bar{\nu}_\mu \rightarrow \bar{\nu}_\mu$	ν STORM

Table 4: A summary of current and future sterile neutrino oscillation experiments.

6.2 Future Experiments

A summary of future sterile neutrino experiments is provided in Table 4.

6.2.1 Pion Decay in Flight

Muon neutrinos (antineutrinos) from positive (negative) pion DIF can be used to search for (anti)neutrino disappearance and electron (anti)neutrino appearance in the sterile neutrino region of interest. Given the usual neutrino energies for these experiments ($\mathcal{O}(1 \text{ GeV})$), the baseline for such an experiment can be considered “short” ($\mathcal{O}(100\text{-}1000 \text{ m})$).

The BNB at Fermilab will provide pion-induced neutrinos to the MicroBooNE LArTPC-based detector starting in 2014 [72]. MicroBooNE will probe the MiniBooNE low energy anomaly [92] with a ~ 90 ton active volume about 100 meters closer to the neutrino source than MiniBooNE. Some coverage of the LSND allowed region in neutrino-mode is also expected, along with LArTPC development and needed precision neutrino-argon cross section measurements [93]. A design involving two LArTPC-based detectors in a near/far configuration, with MicroBooNE as the near detector, is also being considered for deployment in the BNB at Fermilab [75]. A similar two detector configuration in the CERN-SPS neutrino beam has recently been proposed [76]. Two identical LArTPCs, in combination with magnetized spectrometers, would measure the mostly pion DIF induced muon neutrino composition of the beam as a function of distance (300 m, 1600 m) to probe electron neutrino appearance in the sterile neutrino parameter space.

Another BNB-based idea calls for a significant upgrade to the MiniBooNE experiment in which the current MiniBooNE detector becomes the 540 m baseline far detector in a two detector configuration and a MiniBooNE-like oil-based near detector is installed at a baseline of 200 m [74]. Such a configuration could significantly reduce the now largely irreducible systematics associated with MiniBooNE-far-only, mainly coming from neutral pion background events and flux uncertainty. In conjunction with MicroBooNE, “BooNE” could provide a sensitive study of LSND-like electron (anti)neutrino appearance, (anti)muon neutrino disappearance, and the MiniBooNE low energy anomaly.

A low energy 3-4 GeV/c muon storage ring could deliver a precisely known flux of electron neutrinos for a muon neutrino appearance search in the parameter space of interest for sterile neutrinos [77]. The magnetized MINOS-like detectors, envisioned at 20-50 m (near) and ~ 2000 m (far), would need to be magnetized in order to differentiate muon neutrino appearance from intrinsic muon antineutrinos created from the positive muon decay. Similar to most pion DIF beams, the muon storage ring could run in both neutrino-mode and antineutrino-mode. Such an experiment would also provide a technological demonstration of a muon storage ring with a “simple” neutrino factory [94].

6.2.2 Pion or Kaon Decay at Rest

As discussed above, neutrinos from pion DAR and subsequent daughter muon DAR, with their well known spectrum, provide a source for an oscillation search. Notably, LSND employed muon antineutrinos from the pion daughter’s muon DAR in establishing their 3.8σ excess consistent with electron antineutrino appearance.

The 1 MW Spallation Neutron Source at Oak Ridge National Laboratory, a pion and muon DAR neutrino source, in combination with an LSND-style detector could directly probe the LSND excess with a factor of 100 lower steady-state background and higher beam power [80]. A 1 MW source at a large liquid scintillator detector is also under consideration [91]. Such an experiment could reconstruct appearance and disappearance oscillation waves across a ~ 50 m length of detector.

If higher energy proton beams are targeted, then positive kaon DAR and the resulting monoenergetic (235.5 MeV) muon neutrino can also be used to search for sterile neutrinos through an electron neutrino appearance search with a LArTPC-based device [82]. An intense >3 GeV kinetic energy proton beam is required for such an experiment so as to produce an ample number of kaons per incoming proton.

6.2.3 Unstable Isotopes

The disappearance of electron antineutrinos from radioactive isotopes is a direct probe of the reactor/gallium anomaly and an indirect probe of the LSND anomaly. As such neutrinos are in the ones-of-MeV range, the baseline for these experiments is generally on the order of tens of meters or so. Oscillation waves within a single detector can be observed if the neutrinos originate from a localized source, if the oscillation length is short enough, and if the detector has precise enough vertex resolution.

The IsoDAR concept [86] calls for an intense 60 MeV proton source in combination with a kiloton-scale scintillation-based detector for sensitivity to the sterile neutrino. Such a source is being developed concurrently with the DAE δ ALUS experiment, nominally a search for non-zero δ_{CP} [95]. Cyclotron-produced 60 MeV protons impinge on a beryllium-based target, mainly acting as a copious source of neutrons, which is surrounded by an isotopically pure shell of ^7Li . ^8Li , created via neutron capture on ^7Li inside the shell, decays to a 6.4 MeV mean energy electron antineutrino. Placing such an antineutrino source next to an existing detector such as KamLAND [3] could quickly provide discovery-level sensitivity in the reactor anomaly allowed region. Furthermore, ISODAR has the ability to distinguish between one and multiple sterile neutrinos.

Another unstable isotope based idea involves the deployment of a radioactive source inside an existing kiloton-scale detector [85] such as Borexino [96], KamLAND [3], or SNO+ [97]. Electron antineutrinos from a small-extent, ~ 2 PBq ^{144}Ce or ^{106}Ru beta source can be used to probe the sterile

neutrino parameter space. For currently favored parameters associated with sterile neutrino(s), such antineutrinos are expected to disappear and reappear as a function of distance and energy inside of the detector, much like the IsoDAR concept described above.

6.2.4 Nuclear Reactor

A nuclear reactor can be used as a source for an electron antineutrino disappearance experiment with sensitivity to sterile neutrino(s). The Nucifer detector will likely be the first reactor-based detector to test the sterile neutrino hypothesis using antineutrino energy shape rather than just rate [87]. The experiment will take data in 2012/2013. The idea is to place a 1 m³-scale Gd-doped liquid scintillator device within a few tens of meters of a small-extent 70 MW research reactor in an attempt to observe antineutrino disappearance as a function of energy. The observation of an oscillation wave at high- Δm^2 would be unambiguous evidence for the existence of at least one sterile neutrino. Cosmic ray interactions and their products represent the largest source of background for this class of experiment.

One of the challenges of a reactor-based search is the need for a relatively small reactor size, given the baseline required for maximal sensitivity to $\Delta m_{ij}^2 \sim 1 \text{ eV}^2$; a large neutrino source size relative to the neutrino baseline smears L and reduces Δm_{ij}^2 resolution. A sterile search at a GW-scale power reactor is possible, however. The SCRAAM experiment (see Ref. [23]) calls for a Gd-doped liquid scintillator detector at the San Onofre Nuclear Generation Station.

6.2.5 Neutral Current Based Experiments

All of the future experiments previously discussed involve either disappearance or appearance of neutrinos and antineutrinos detected via the charged current. A NC-based disappearance experiment provides unique sensitivity to the sterile neutrino, however. In case a disappearance was observed in a NC experiment, one would know that the active flavor neutrino(s) in question had oscillated into the non-interacting sterile flavor. Specifically, such an experiment would provide a measure of $|U_{s4}|$, the sterile flavor composition of the fourth neutrino mass eigenstate, and definitively prove the existence of a sterile flavor neutrino, especially when considered in combination with CC based experiments. A full understanding of the mixing angles associated with sterile neutrino(s) will require a NC based experiment. The Ricochet concept [84] calls for oscillometry measurements using NC coherent neutrino-nucleus scattering detected via low temperature bolometers [78, 79, 84]. Both reactor and isotope decay sources are being considered for these measurements, utilizing the as-yet-undetected coherent neutrino-nucleus scattering process.

7 Conclusions

This paper has presented results of SBL experiments discussed within the context of oscillations involving sterile neutrinos. Fits to (3+1), (3+2), and (3+3) models have been presented. We have examined whether the (3+3) model addresses tensions observed with (3+1) and (3+2) fits.

Several issues arise when comparing data sets in (3+1) and (3+2) models. In a (3+1) model, the compatibility of the neutrino vs. antineutrino data sets is poor (0.14%), and the compatibility among all data sets is only 0.043%. In a (3+2) model, there is a striking disagreement between appearance and disappearance data sets, with a compatibility of 0.0082%.

A (3+3) model fit achieves a compatibility of 90% among all data sets. The χ^2 -probability for the best fit is 67%, compared to 2.1% for the null (no oscillations) scenario. Though this value is on the order of the χ^2 -probabilities found in (3+1) and (3+2) models, at 55% and 69%, respectively, the (3+3) fit resolves the incompatibility issues seen in (3+1) and (3+2) models, with the exception of the MiniBooNE appearance data sets. Therefore, we argue that (3+3) (and possibly (3+2)) fits should be the main focus of sterile neutrino phenomenological studies in the future.

While the indications of sterile neutrino oscillations have historically been associated with only appearance-based SBL experiments, the recently realized suppression in observed $\bar{\nu}_e$ disappearance reactor experiments provides further motivation for these models. As we have shown one can consistently fit most results under the same, (3+3) hypothesis with improved compatibility. However, the need for additional information from both appearance and disappearance experiments provides strong motivation for pursuing the future experiments discussed in this paper.

Acknowledgments

We thank William Louis and Zarko Pavlovic for valuable discussions. We thank the National Science Foundation for their support.

References

- [1] K. Abe *et al.* (Super-Kamiokande Collaboration), Phys. Rev. D **83**, 052010 (2011).
- [2] B. Aharmim *et al.* (SNO Collaboration), Phys. Rev. C **81**, 055504 (2010).
- [3] S. Abe *et al.* (KamLAND Collaboration), Phys. Rev. Lett. **100**, 221803 (2008).
- [4] R. Wendell *et al.* (Kamiokande Collaboration), Phys. Rev. D **81**, 092004 (2010).
- [5] W.W.M. Allison *et al.* (Soudan-2 Collaboration), Phys. Rev. D **72**, 052005 (2005).
- [6] M.H. Ahn *et al.* (K2K Collaboration), Phys. Rev. D **74**, 072003 (2006).
- [7] D.G. Michael *et al.* (MINOS Collaboration), Phys. Rev. Lett. **97**, 191801 (2006).
- [8] P. Adamson *et al.* (MINOS Collaboration), Phys. Rev. D **77**, 072002 (2008).
- [9] P. Adamson *et al.* (MINOS Collaboration), Phys. Rev. Lett. **101**, 131802 (2008).
- [10] P. Adamson *et al.* (MINOS Collaboration), Phys. Rev. Lett. **106**, 181801 (2011).
- [11] P. Adamson *et al.* (MINOS Collaboration), Phys. Rev. Lett. **107**, 021801 (2012).
- [12] P. Adamson *et al.* (MINOS Collaboration), Phys. Rev. Lett. **107**, 181802 (2011).
- [13] K. Abe *et al.* (T2K Collaboration), Phys. Rev. Lett. **107**, 041801 (2011).
- [14] Y. Abe *et al.* (Double Chooz Collaboration), Phys. Rev. Lett. **108**, 131801 (2012).
- [15] F.P. An *et al.* (Daya Bay Collaboration), Phys. Rev. Lett. **108**, 171803 (2012).
- [16] J. Ahn *et al.* (RENO collaboration), Phys. Rev. Lett. **108**, 191802 (2012).
- [17] A. Aguilar-Arevalo *et al.* (LSND Collaboration), Phys. Rev. D **64**, 112007 (2001).
- [18] A. Aguilar-Arevalo *et al.* (MiniBooNE Collaboration), To be submitted to Phys. Rev. Lett. (2012).
- [19] G. Mention, M. Fechner, T. Lasserre, T. Mueller, D. Lhuillier, *et al.*, Phys. Rev. D **83**, 073006 (2011).
- [20] M. Sorel, J.M. Conrad and M. Shaevitz, Phys. Rev. D **70**, 073004 (2004).
- [21] G. Karagiorgi, A. Aguilar-Arevalo, J. Conrad, M. Shaevitz, K. Whisnant, *et al.*, Phys. Rev. D **5**, 013011 (2007).

- [22] G. Karagiorgi, Z. Djurcic, J.M. Conrad, M.H. Shaevitz and M. Sorel, Phys. Rev. D **80**, 073001 (2009).
- [23] K.N. Abazajian *et al.*, arXiv:1204.5379 [hep-ph] (2012) .
- [24] M. Maltoni and T. Schwetz, Phys. Rev. D **76**, 093005 (2007).
- [25] ALEPH Collaboration, DELPHI Collaboration, L3 Collaboration, OPAL Collaboration, SLD Collaboration, LEP Electroweak Working Group, SLD Electroweak and Heavy Flavour Groups, Phys. Rept. **427**, 257 (2006).
- [26] A.A. Aguilar-Arevalo and others (MiniBooNE Collaboration), Phys. Rev. Lett. **105**, 181801 (2010).
- [27] M. A. Acero, C. Giunti, and M. Laveder, Phys. Rev. D **78**, 073009 (2008).
- [28] J. Dunkley, R. Hlozek, J. Sievers, V. Acquaviva, P. Ade, *et al.*, Astrophys. J. **739**, 52 (2011).
- [29] M. Gonzalez-Garcia, M. Maltoni, and J. Salvado, JHEP **1008**, 117 (2010).
- [30] E. Giusarma, M. Archidiacono, R. de Putter, A. Melchiorri, and O. Mena, Phys. Rev. D **85**, 083522 (2012).
- [31] J. Hamann, S. Hannestad, G. G. Raffelt, and Y. Y. Wong, JCAP **1109**, 034 (2011).
- [32] G. Karagiorgi, M. H. Shaevitz, and J. M. Conrad, arXiv:1202.1024 [hep-ph] (2012) .
- [33] J. Abdurashitov *et al.* (SAGE Collaboration), Phys. Rev. C **80**, 015807 (2009).
- [34] F. Kaether, W. Hampel, G. Heusser, J. Kiko, and T. Kirsten, Phys. Lett. B **685**, 47 (2010).
- [35] C. Jones, PhD Thesis, Massachusetts Institute of Technology (2012).
- [36] T. Mueller, D. Lhuillier, M. Fallot, A. Letourneau, S. Cormon, *et al.*, Phys. Rev. C **83**, 054615 (2011).
- [37] P. Huber, Phys. Rev. C **84**, 024617 (2011).
- [38] R. Burman and F. K. T. und Umwelt, *Neutrino Fluxes at KARMEN from Pion Decay in Flight* (FZKA, 1996).
- [39] R. Burman, M. Potter, and E. Smith, Nucl. Instrum. Meth. A **291**, 621 (1990).
- [40] A.A. Aguilar-Arevalo *et al.* (MiniBooNE Collaboration), Phys. Rev. D **79**, 072002 (2009).
- [41] S. E. Kopp, Phys. Rept. **439**, 101 (2007).
- [42] M. Catanesi *et al.* (HARP Collaboration), Nucl. Instrum. Meth. A **571**, 527 (2007).
- [43] N. Graf *et al.* (MIPP Collaboration), Nucl. Instrum. Meth. A **615**, 27 (2010).
- [44] J. Conrad and M. Shaevitz, Phys. Rev. D **85**, 013017 (2012).

- [45] B. Armbruster *et al.* (KARMEN Collaboration), Phys. Rev. D **65**, 112001 (2002).
- [46] A.A. Aguilar-Arevalo *et al.* (MiniBooNE Collaboration), In Preparation .
- [47] A. Aguilar-Arevalo *et al.* (MiniBooNE Collaboration), Phys. Rev. D **78**, 012007 (2008).
- [48] A. A. Aguilar-Arevalo *et al.* (MiniBooNE Collaboration), Phys. Rev. Lett. **103**, 061802 (2009).
- [49] P. Adamson *et al.* (MiniBooNE and MINOS Collaborations), Phys. Rev. Lett. **102**, 211801 (2009).
- [50] P. Astier *et al.* (NOMAD Collaboration), Phys. Lett. B **570**, 19 (2003).
- [51] I. Stockdale, A. Bodek, F. Borcharding, N. Giokaris, K. Lang, *et al.*, Z. Phys. C **27**, 53 (1985).
- [52] F. Dydak, G. Feldman, C. Guyot, J. Merlo, H. Meyer, *et al.*, Phys. Lett. B **134**, 281 (1984).
- [53] D. Casper, Nucl. Phys. Proc. Suppl. **112**, 161 (2002).
- [54] Y. Declais, J. Favier, A. Metref, H. Pessard, B. Achkar, *et al.*, Nucl. Phys. B **434**, 503 (1995).
- [55] C. Giunti and M. Laveder, Phys. Rev. C **83**, 065504 (2011).
- [56] A. Esmaili, F. Halzen, and O. Peres, arXiv:1206.6903 [hep-ph] (2012) .
- [57] P. Adamson *et al.* (MINOS collaboration), arXiv:1202.2772 [hep-ex] (2012) .
- [58] P. Adamson *et al.* (MINOS Collaboration), arXiv:1108.1509 [hep-ex] (2012) .
- [59] M. Maltoni, T. Schwetz, M. Tortola, and J. Valle, New J. Phys. **6**, 122 (2004).
- [60] K. K. M. Honda, T. Kajita and S. Midorikawa, Phys. Rev. D **70**, 043008 (2004).
- [61] M. C. Gonzalez-Garcia and M. Maltoni, Phys. Rev. D **70**, 033010 (2004).
- [62] S.H. Ahn *et al.* (K2K Collaboration), Phys. Lett. B **511**, 178 (2001).
- [63] M.H. Ahn *et al.* (K2K Collaboration), Phys. Rev. Lett. **041801**, 90 (2003).
- [64] M.H. Ahn *et al.* (K2K Collaboration), Phys. Rev. D **072003**, 74 (2006).
- [65] P. Brâemaud, *Markov chains: Gibbs fields, Monte Carlo simulation, and queues* (Springer, New York, 1999).
- [66] M. Maltoni and T. Schwetz, Phys. Rev. D **68**, 033020 (2003).
- [67] J. Kopp, M. Maltoni, and T. Schwetz, Phys. Rev. Lett. **107**, 091801 (2011).
- [68] C. Giunti and M. Laveder, Phys. Lett. B **706**, 2007 (2011).
- [69] A. Donini, P. Hernandez, J. Lopez-Pavon, M. Maltoni, and T. Schwetz, arXiv:1205.5230 [hep-ph] (2012) .
- [70] M. Matrini and M. Ericson and G. Chanfray, arXiv:1202.4745v2 [hep-ph] (2012) .

- [71] C. H. J. A. Harvey and R. Hill, Phys. Rev. Lett **99**, 261601 (2007).
- [72] H. Chen *et al.* (MicroBooNE Collaboration), “Proposal for a New Experiment Using the Booster and NuMI Neutrino Beamlines: MicroBooNE” (2007) .
- [73] G. Tzanakos *et al.* (MINOS+ Collaboration), “MINOS+: a Proposal to FNAL to run MINOS with the medium energy NuMI beam, Tech. Rep.” (2011) .
- [74] I. Stancu *et al.*, “A Proposal to Build a MiniBooNE Near Detector: BooNE” (2011) .
- [75] G. Karagiorgi, “Proceedings of TIPP 2011” (2011) .
- [76] C. Rubbia *et al.*, “A comprehensive search for anomalies from neutrino and anti-neutrino oscillations at large mass difference with two LArDTPC imaging detector at different distances from the CERN-PS, Tech. Rep.” (2011) .
- [77] P. Kyberd *et al.*, arXiv:1206.0294 [hep-ex] (2012) .
- [78] A.J. Anderson, J.M. Conrad, E. Figueroa-Feliciano, K. Scholberg, and J. Spitz, Phys. Rev. D **84**, 113008 (2011).
- [79] A.J. Anderson, *et al.*, arXiv:1201.3805 [hep-ph] (2012) .
- [80] I. Stancu *et al.* (OscSNS Collaboration), “The OscSNS White Paper” (2008) .
- [81] S.K. Agarwalla and P. Huber, Phys. Lett. B **696**, 359 (2011).
- [82] J. Spitz, Phys. Rev. D **85**, 093020 (2012).
- [83] C. Grieb, J. Link, and R.S. Raghavan, Phys. Rev. D **75**, 093006 (2007).
- [84] J. Formaggio, E. Figueroa-Feliciano, A.J. Anderson , Phys. Rev. D **85**, 013009 (2012).
- [85] M. Cribier *et al.*, Phys. Rev. Lett. **107**, 201801 (2011).
- [86] A. Bungau *et al.*, arXiv:1205.4419 [hep-ex] (2012) .
- [87] A. Porta *et al.*, IEEE Transactions on Nuclear Science **57**, 2732 (2010).
- [88] A. Serebrov, arXiv:1205.2955 [hep-ph] (2012) .
- [89] S. Gninenko, Phys. Rev. D **85**, 051702 (2012).
- [90] A. Aguilar-Arevalo *et al.* (MiniBooNE Collaboration), arXiv:1206.6915 [hep-ph] (2012) .
- [91] S.K. Agarwalla, J.M. Conrad, and M.H. Shaevitz, JHEP **1112**, 085 (2011).
- [92] A.A. Aguilar-Arevalo *et al.* (MiniBooNE Collaboration), Phys. Rev. Lett. **102**, 101802 (2009).
- [93] C. Anderson *et al.* (ArgoNeuT Collaboration), Phys. Rev. Lett. **108**, 161802 (2012).
- [94] S. Geer, Phys. Rev. D **57**, 6989 (1998).

- [95] J.M. Conrad and M.H. Shaevitz, Phys. Rev. Lett. **104**, 141802 (2010).
- [96] G. Alimonti *et al.* (Borexino Collaboration), Astropart. Phys. **16**, 205 (2002).
- [97] M. Chen, Nucl. Phys. Proc. Suppl. **145**, 65 (2005).